Nonlinear Interferometry: A New Approach for Imaging and Sensing

Jorge Fuenzalida, Enno Giese, and Markus Gräfe*

Nonlinear interferometers are a ubiquitous tool in quantum photonics. As such, they allow spooky-like imaging with undetected light. On the one side their working principle is based on the principle of induced coherence, which is deeply rooted in the heart of quantum mechanics. On the other side, they bear the strong potential to serve as new tool for biomedical imaging. In this review, an extensive overview about nonlinear interferometers and their working principle is given. A particular focus is set on their exploitation for quantum imaging and sensing. In addition, related side topics and further application fields as well as perspectives are provided.

1. Introduction

Optical imaging and sensing is a major tool in biomedical diagnosis, life sciences, and material analysis. Hence, a multitude of techniques ranging from simple widefield light microscopy[1] over Fourier-transform infrared hyperspectral imaging[2] to super-resolution techniques like photoactivated localization microscopy[3] have been developed in the past. This continuous progress was always driven by the goal to overcome the state of the art, to go beyond the current limitations one faces. This spirit has not disappeared and still persists today. While former approaches exploited the wave- or particle-nature of light, new strategies utilize the quantum properties of light. In going beyond classical electrodynamics, new imaging and sensing features become possible.[4,5] As already experimentally demonstrated, non-classical states of light allow for super-resolution imaging,[6,7] sub-shot-noise sensing,[8,9] and super-sensitive Fluorescence detection.[10,11] In addition, a very promising method based on nonlinear interferometers allows to illuminate a sample with light that remains undetected, while the object's image is obtained with light that does not interact with it. This is referred

to as "quantum imaging/sensing with undetected light."[12] For this technique nonlinear interferometers and the effect of "induced coherence" are exploited.[13,14] Here, the indistinguishability of photon pair generation sources allows this kind of spooky sensing scheme. Naturally, it offers a great advantage to perform imaging and sensing in spectral domains, where direct detection is physically or technically difficult. A prominent example would be sensing in the mid-infrared spectral domain, where detection is challenging due to either the unavailability of detection systems or detection systems with low detection efficiency, low signal-to-noise ratio, and high costs. This challen can be circumvented with nonlinear interferometers, where sample interaction is carried out with the mid-infrared light that is not detected. At the same time, detection is performed with visible light that does not interact with the sample and benefits from low cost, high efficiency, and high signal-to-noise ratio of silicon-based detectors. In this vein, nonlinear interferometers can serve as workhorse not only for fundamental quantum physics[15–17] but also for quantum imaging, even at video rate,[18] quantum microscopy,[19,20] spectroscopy,[21] optical coherence tomography,[22,23] THz sensing,[24,25] holography,[26,27] and image distillation.[28] Based in the rapid physical-technological development, new tools for biomedical sensing or material science can be envisioned, such as label-free chemical selective bioimaging with visible light.

To elaborate on the many different aspects of nonlinear interferometers for quantum imaging and sensing, this review is structured as follows: First, we provide fundamentals of nonlinear interferometers by explaining the process of photon pair generation, the principle of induced coherence and discuss the different types of nonlinear interferometers that have been developed. This is followed by three sections on quantum imaging with undetected light focusing on the general principle of image formation due to spatial (momentum) correlations, extending this description to position correlations and finally discussing the spatial resolution obtainable in such systems. Section 6 is devoted to quantum holography and associated image distillation. It is followed by a section on exploiting extreme spectral ranges in terms of spectroscopy, optical coherence tomography, and THz sensing, as well as utilizing polarization as an additional degree of freedom for quantum state tomography. The review is closed with a section on additional and open topics such as high parametric-gain regime, including a discussion on the role of stimulating the emission with one or two fields and by sketching future perspectives.

J. Fuenzalida, E. Giese, M. Gräfe
Institute for Applied Physics
Technical University of Darmstadt
Schloßgartenstraße 7, 64289 Darmstadt, Germany
E-mail: markus.graefe@tu-darmstadt.de

ADVANCED
SCIENCE NEWS

www.advancedsciencenews.com

ADVANCED
QUANTUM
TECHNOLOGIES

www.advquantumtech.com
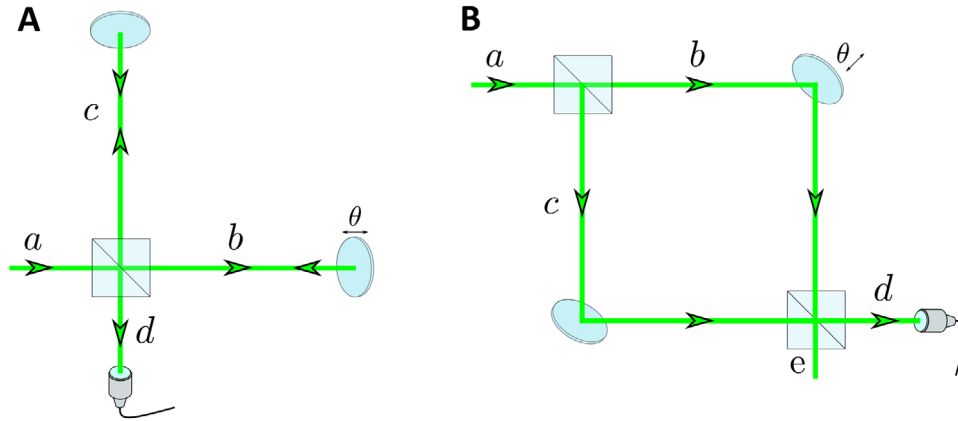
Figure 1. Optical interferometer configurations. A) Michelson and B) Mach–Zehnder.

2. Fundamentals of Nonlinear Interferometers

2.1. Optical Interferometer

Interferometers are essential devices that help to observe wave-particle duality in a controlled manner. The first documented interferometer was invented by A. A. Michelson back in 1891, and a modern version of it is depicted in **Figure 1A**. The "Michelson interferometer" has one beam splitter component that works as an input and output and two internal paths that the beams travel forward and then backward. When the beams are recombined, if there is no "path information," the outcoming beams behave as waves and interfere. An alternative interferometric configuration is shown in Figure 1B and is known as the "Mach–Zehnder interferometer." The main difference in the latter interferometer is that different beam splitters serve as input and output. Although there are many other interferometric configurations, the two introduced here are relevant in this review.

2.2. Spontaneous Parametric Down-Conversion

Spontaneous parametric down-conversion (SPDC) is a well-known process to produce photon pairs carrying non-classical properties (**Figure 2**). SPDC was theoretically introduced by D. Klishko[29] and experimentally realized by D. C. Burnham and D. L. Weinberg.[30] The properties of photon pairs produced in SPDC processes have been extensively studied in terms of their

spatial properties[31] or for the generation of entanglement in two[32] and high dimensions.[33]
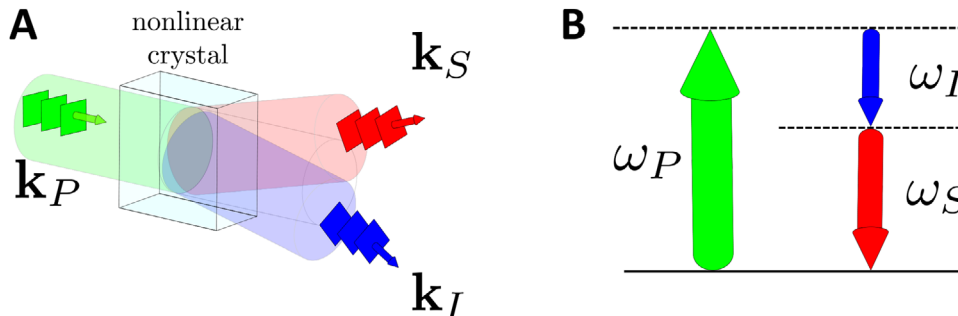
In this review, we mainly present results within the paraxial regime, where the wavelengths of the photons involved in the SPDC process are much smaller than the crystal length, and the angles of the pump beam and both SPDC photons are small. However, we briefly discuss results in the non-paraxial regime when necessary. In the paraxial regime, considering signal and idler photons are emitted in the same polarization mode, the bi-photon state is

$$|\psi\rangle_{\text{SPDC}} = \int d\omega_I \, d\omega_S \, d\mathbf{q}_I \, d\mathbf{q}_S \, C(\mathbf{q}_I, \mathbf{q}_S, \omega_I, \omega_S) \, |\mathbf{q}_I, \omega_I\rangle \, |\mathbf{q}_S, \omega_S\rangle \tag{1}$$
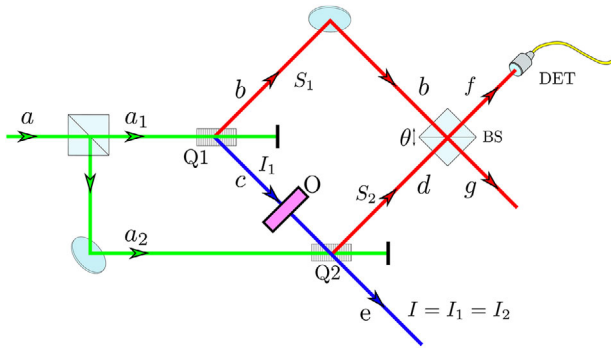
where $|\mathbf{q}_I, \omega_I\rangle$ ($|\mathbf{q}_S, \omega_S\rangle$) represents a one-photon state of the idler (signal) photon with a transverse wave vector $\mathbf{q}_I$ ($\mathbf{q}_S$) and frequency ω_I (ω_S). The function C is a joint amplitude density of modes for signal and idler photons which can be represented by[32]

$$C \propto \mathscr{A}(|\mathbf{q}_I + \mathbf{q}_S|^2) \, S(\omega_I + \omega_S) \, \text{sinc}\left\{ \frac{L_z \, \Delta k_z}{2} + \mathcal{F}(\mathcal{T}, \lambda) \right\} \tag{2}$$

where $\mathscr{A}$ is the angular spectrum of the pump beam, S is the spectral density function, L_z is the length of the nonlinear medium, and Δk_z is the longitudinal wave mismatch. For the representation of Δk_z in degenerate and non-degenerate processes,

Figure 2. Phase matching conditions in SPDC. A) Momentum conservation and B) energy conservation.

**ADVANCED
SCIENCE NEWS**
www.advancedsciencenews.com

**ADVANCED
QUANTUM
TECHNOLOGIES**
www.advquantumtech.com

Figure 3. Induced coherence. A photon pair is emitted in a quantum superposition of sources Q1 and Q2. Pump beam, signal, and idler paths are denoted by green, blue, and red lines. Through the alignment of the idlers and recombination of the signals, the which-source information is erased and, consequently, coherence is induced on the signal photon. This results in a single-photon interference of signals. If an object is placed in the idler path, then, the signal photon visibility is directly proportional to the object transmission. O, object; BS, beam splitter; DET, detector.

see refs. [34] and [35], respectively. $\mathcal{F}$ is the collinear phase-mismatch parameter relating the wavelengths, the crystal temperature $\mathcal{T}$, and the refractive indices in the SPDC process that are determined by the crystal Sellmeier equation.[36] By changing the crystal temperature, the SPDC cones can be varied from collinear to noncollinear emission.

2.3. Induced Coherence without Induced Emission

The 1980s and 1990s were prominent years for quantum optics. During these years several quantum effects were discovered that have helped the development of novel technologies based on quantum physics, the so-called "quantum technologies." This progress was fuelled by several groups, with essential contributions from Europe and the United States. A clear example is given by the group led by Leonard Mandel at the University of Rochester, famous for introducing the Hong-Ou-Mandel effect[37,38] and the induced coherence without induced emission (ICIE) effect,[13,14] among other relevant works.[39–41] The ICIE effect was one of the first experimental implementations of an optical nonlinear interferometer. This effect also forms one basis of the following experiments presented in this review.

2.3.1. Zou–Wang–Mandel Interferometer

Induced coherence without induced emission is a quantum interference effect where due to the lack of "which-source information"[42] of a photon pair emission in two independent processes, single-photon interference is observed. The which-source information can be erased in two different ways, temporally or spatially. In the implementation done by Mandel's group, spatial indistinguishability is used, see **Figure 3**. We called this configuration as Zou–Wang–Mandel (ZWM) interferometer. To explain ICIE further, let us start by considering two photons, namely, signal (S) and idler (I), produced in a spontaneous parametric down-conversion process. Moreover, by pumping coherently the two spatially separated sources Q1 and Q2, one photon

pair is emitted in a quantum superposition as

$$|\Psi\rangle = \frac{1}{\sqrt{2}} \left(|I_1\rangle |S_1\rangle + e^{i\theta} |I_2\rangle |S_2\rangle \right) \tag{3}$$

where θ is an interferometric phase, and the subscripts 1 and 2 correspond to the sources Q1 and Q2, respectively. By the suggestion of Jeff Ou, the idler photon emitted in Q1 was aligned with the idler photon emitted in Q2. This way, after Q2, idler photons were indistinguishable, i.e., $|I_1\rangle = |I_2\rangle = |I\rangle$. Additionally, signal photons emitted at sources Q1 and Q2 are recombined in a beam splitter and collected by a detector placed in path f. Therefore, under the idlers alignment consideration, and from Equation (3), the normalized signal photon count rate (intensity) is approximated to

$$\langle N_S \rangle \propto [1 + \cos(\theta)] \tag{4}$$

implying that the signal photon emitted either in Q1 or Q2 is interfering with itself (single-photon interference). This is only possible because the idler photon has been aligned, and therefore, it has induced coherence on its partner signal. In the same experiment,[13] the fact that the idler is inducing coherence in the signal was corroborated by introducing an object with a complex amplitude transmission T in path c, in between sources Q1 and Q2. In this case, the signal photon visibility was directly proportional to the transmission of the object
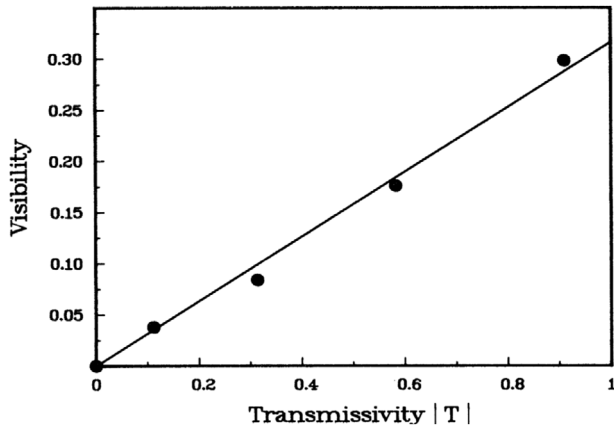
$$\mathcal{V}_S = \frac{\langle N_S \rangle_{\max} - \langle N_S \rangle_{\min}}{\langle N_S \rangle_{\max} + \langle N_S \rangle_{\min}} \tag{5}$$

$$\mathcal{V}_S = |T| \tag{6}$$

$\langle N_S \rangle_{\max}$ ($\langle N_S \rangle_{\min}$) is the maximum (minimum) intensity of the signal. Thus an object placed in path c introduces which-source information of the idlers emission and destroys the coherence induced on the signals. We can understand this considering an additional detector located in path e collecting idlers (D_I). Initially, without the presence of an object and considering lossless components, the detector D_I collects an equal number of idlers emitted from both sources Q1 and Q2. Then by introducing the object in path c the counts in D_I will decrease, reaching a minimum of half of the initial counts. Since every idler from Q2 is still being collected by D_I, the diminishing in counts can only be associated with the absorption of idler photons emitted in Q1 before reaching Q2. Therefore, depending on the transmission amplitude of the object, D_I "knows" from which source the idler photon was emitted. This is always true, independent if the idler photon is detected or not.

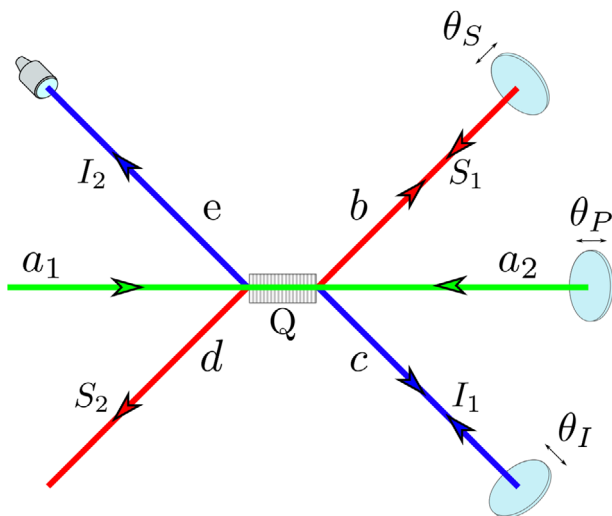### 2.3.2. SU(1,1) Interferometer

The SU(1,1) interferometer was theoretically introduced by B. Yurke, S. L. McCall, and J. R. Klauder in ref. [43]. This nonlinear interferometer uses a nonlinear medium as an input/output and is conceptually different from the ZWM interferometer. However, the ZWM and SU(1,1) interferometers have many similarities in the low-gain regime. For example, in both configurations,

**ADVANCED
SCIENCE NEWS**

www.advancedsciencenews.com

**ADVANCED
QUANTUM
TECHNOLOGIES**

www.advquantumtech.com

Figure 4. Visibility depending on transmissivity. Consider a transmissive object placed in the idler path between the sources Q1 and Q2. The transmissivity of this object and the visibility of the signal photon are directly proportional, i.e., $\mathcal{V}_S = |T|$. Reproduced with permission.[13] Copyright 1991 The American Physical Society.

it can be observed the ICIE effect followed by the same or similar outputs. Nevertheless, this changes in the high-gain regime; we expand these differences in Section 8.1.

One of the early implementations of an SU(1,1) interferometer was introduced in the 1990s by the group of Anton Zeilinger in ref. [15], see **Figure 5**. This configuration exploits the temporal indistinguishability in the emission of a photon pair. In this interferometer, a first photon pair (S_1, I_1) can be generated in the forward propagation of the pump beam (a_1) into the paths b and c, see Figure 5. After the pump beam is reflected by its end mirror, a second photon pair can be generated in the backward direction (a_2), into the paths e and d. Therefore, in order to see interference, one needs to erase the "which-time information" of the photon pair.

Figure 5. SU(1,1) interferometer. Induced coherence also can be obtained through temporal indistinguishability. A photon pair can be created in the forward (a_1) or backward (a_2) directions.

Continuing in the low-gain regime, let us analyze similarities and differences of the ICIE effect in the ZWM and SU(1,1) interferometers. The first difference is that in the SU(1,1) interferometer both photons (signal and idler) show single-photon interference, whereas in the ZWM interferometer only the signal photon does. The second difference is the effect of an object in visibility; in a ZWM interferometer the object transmission is proportional to the visibility, $\mathcal{V}_S = |T|$. In the case of an SU(1,1) interferometer, this depends on where the object is located. If the object is located at the idler's end mirror, then the same relation is obtained: $\mathcal{V}_S = |T|$. However, if the object is not placed at the end mirror, then the idler passes twice through the object, and the visibility changes to $\mathcal{V}_S = |T|^2$.[18]

2.3.3. Quantum Indistinguishability and Frequencies Relationship in Induced Coherence

In order to observe quantum interference, the optical paths must fulfill the following conditions.[14,44] In the ZWM interferometer,
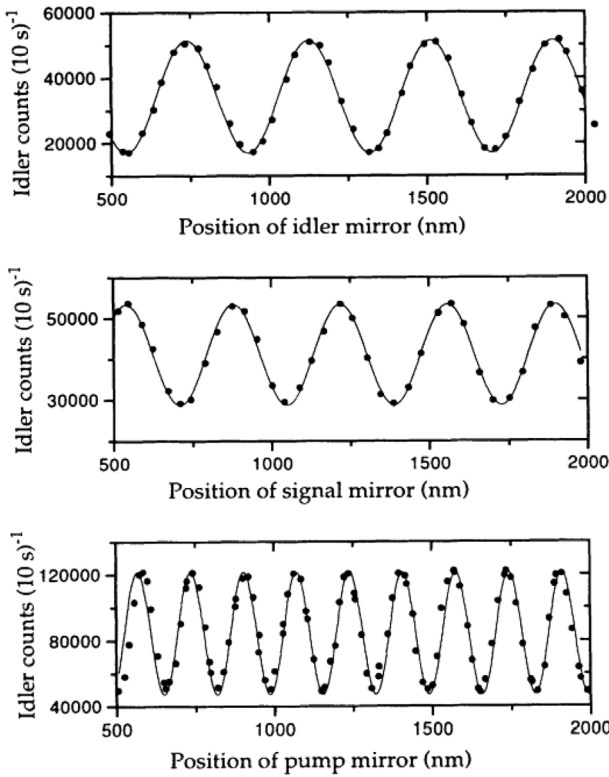
$$|l_{Sb} - l_{Sd} - l_{Ic}| \ll L_{SI} \tag{7}$$

where l_{Sb} and l_{Sd} are the optical path lengths of the signal in b and d, respectively; l_{Ic} is the optical path of the idler photon in c. This difference must be smaller than the coherence length of the SPDC photon pair L_{SI}, which is associated with the bandwidth of the photon pair.[14,23,45] Similarly for the SU(1,1) interferometer, we have

$$|l_{Sb} - l_{Ic}| \ll L_{SI} \tag{8}$$

Equations (7) and (8) suffice coherence length conditions if, additionally, a pump beam with a long coherence length is considered. The relation between the three wavelengths involved in a nonlinear interferometer was studied in ref. [15]. They found that the interference periods, which are obtained by changing one of the optical paths θ_S, θ_P, or θ_I in Figure 5, are related to half of the wavelength of the photon traveling in that path, as shown in **Figure 6**. Therefore, this article already showed some potential of induced coherence for applications that were developed many years later.

2.3.4. Early Days Research

In the immediate years after,[13] several groups used these interferometers to study optical coherence properties and fundamental physics. For example, the visibility of the signal photon was studied by changing the optical path of the idler photon[46] and its spatial distribution.[47,48] There also were carried out a series of experiments testing fundamental physical properties such as a frustration/enhancement generation of photon pair emission[15] and the implementation of a quantum eraser (proposed by Scully and Drühl[49]) altogether with the single- and two-photon interference complementarity.[50] In 2000, the first study of induced coherence with and without induced emission was published.[51] This paper paves the way for induced coherence in the high-gain regime.

**ADVANCED
SCIENCE NEWS**

www.advancedsciencenews.com

**ADVANCED
QUANTUM
TECHNOLOGIES**

www.advquantumtech.com

Figure 6. Relative phases in induced coherence. The authors show that the idler photon interference period changes depending on what optical path is varied. In the SU(1,1) interferometer, this corresponds to half of the wavelength of the photon travelling that path. Reproduced with permission.[15] Copyright 1994 The American Physical Society.

3. Quantum Imaging with Undetected Light

Quantum physics and its counterintuitive nature, from time to time, surprise the community with novel and astonishing phenomena and techniques. This is the case of quantum imaging with undetected light (QIUL), an imaging technique introduced by Anton Zeilinger's group in 2014.[12] Here a photon pair emitted in a quantum superposition between two spatially separated sources is employed to image an object using an interferometric scheme. In QIUL, one photon of the photon pair illuminates an object while its partner photon is detected to retrieve its image. The photon illuminating the object is never detected. Therefore, contrary to ghost imaging (GI),[52–58] QIUL does not require coincidences events. In this way, QIUL offers a fundamental detection advantage in comparison to other quantum imaging techniques.[4] The theoretical description of QIUL was introduced in ref. [59]. In this section, we focus on the quantum domain (low-gain regime), but it is worth mentioning that imaging with undetected light also has been implemented classically.[60,61]

3.1. Initial State

The initial state of the photon pair produced in an SPDC process can be expressed in terms of the transverse wave vectors by

$$|\psi\rangle_{SPDC} = \int d\mathbf{q}_I \, d\mathbf{q}_S \, C(\mathbf{q}_I, \mathbf{q}_S) \, |\mathbf{q}_I\rangle \, |\mathbf{q}_S\rangle \qquad (9)$$

where $\mathbf{q}_I$ ($\mathbf{q}_S$) represents the transverse wave vector of the idler (signal) photon. $C(\mathbf{q}_I, \mathbf{q}_S)$ is the joint amplitude of the modes $\mathbf{q}_I$ and $\mathbf{q}_S$, and

$$P(\mathbf{q}_I, \mathbf{q}_S) = |C(\mathbf{q}_I, \mathbf{q}_S)|^2 \qquad (10)$$

is the joint probability of idler and signal photons with transverse momenta $\hbar\mathbf{q}_I$ and $\hbar\mathbf{q}_S$, respectively. We can also write the conditional probability for the idler and signal photons by[62]

$$P(\mathbf{q}_I|\mathbf{q}_S) = \frac{P(\mathbf{q}_I, \mathbf{q}_S)}{P(\mathbf{q}_S)} = \frac{|C(\mathbf{q}_I, \mathbf{q}_S)|^2}{\int d\mathbf{q}_I |C(\mathbf{q}_I, \mathbf{q}_S)|^2} \qquad (11)$$

In this introductory section, the condition of perfect momentum correlation of idler and signal photons is considered, i.e., the phase-matching condition $\mathbf{q}_I + \mathbf{q}_S = \mathbf{q}_P \approx 0$ is fulfilled, where $\mathbf{q}_P$ is the pump's transverse wave vector. In the following sections, we will analyze different scenarios of $C(\mathbf{q}_I, \mathbf{q}_S)$, with some of them directly linked to the spatial resolution.

In QIUL, one photon pair is emitted in a quantum superposition of two spatially separated sources, Q1 and Q2, see **Figure 7**. If the sources Q1 and Q2 are identical and these are pumped coherently with the same characteristics of the pump beam (e.g., pump power, pump waist), then the initial state of QIUL can be represented by

$$|\psi\rangle_{QIUL} = \frac{1}{\sqrt{2}}(|Q1\rangle + e^{i\phi} |Q2\rangle)$$

$$= \frac{1}{\sqrt{2}} \int d\mathbf{q}_I \, d\mathbf{q}_S \, C(\mathbf{q}_I, \mathbf{q}_S) \, [|\mathbf{q}_{I1}\rangle \, |\mathbf{q}_{S1}\rangle + e^{i\phi} |\mathbf{q}_{I2}\rangle \, |\mathbf{q}_{S2}\rangle]$$

$$(12)$$

where ϕ is a phase between the sources.

3.2. Idler Beam Alignment and Field of View Formation

The first implementation of QIUL employs the "momentum anticorrelation" of a photon pair in the image acquisition.[12] Thus, the object is located in the far-field plane from source Q1 of the idler beam, where a point on the object $\mathbf{r}_O = (x_O, y_O)$ is illuminated by an idler photon with transverse momentum $\hbar\mathbf{q}_I$. In a similar way, the camera is located in the far-field plane from source Q2 of the signal beam, where a point on the camera $\mathbf{r}_C = (x_C, y_C)$ detects a signal photon with a transverse momentum $\hbar\mathbf{q}_S$. Due to the perfect momentum anticorrelation considered here, the detection of a signal photon with transverse momentum $\hbar\mathbf{q}_S$, allows us to infer the transverse momentum $\hbar\mathbf{q}_I$ of its idler partner perfectly. Since this is not the only physical way of implementing QIUL, we hereon called momentum based QIUL as M-QIUL for simplicity (**Figure 8**).

Consider that the nonlinear crystal has two transverse dimensions, width and height, and a longitudinal one in the direction of the pump beam propagation, length. If the crystal length is larger than the wavelengths emitted in the SPDC process, its emission angle is considered to be small with respect to the optical axis z. The emission angle forms an emission cone composed of many **k**-vectors, which can be Fourier decomposed into plane waves.
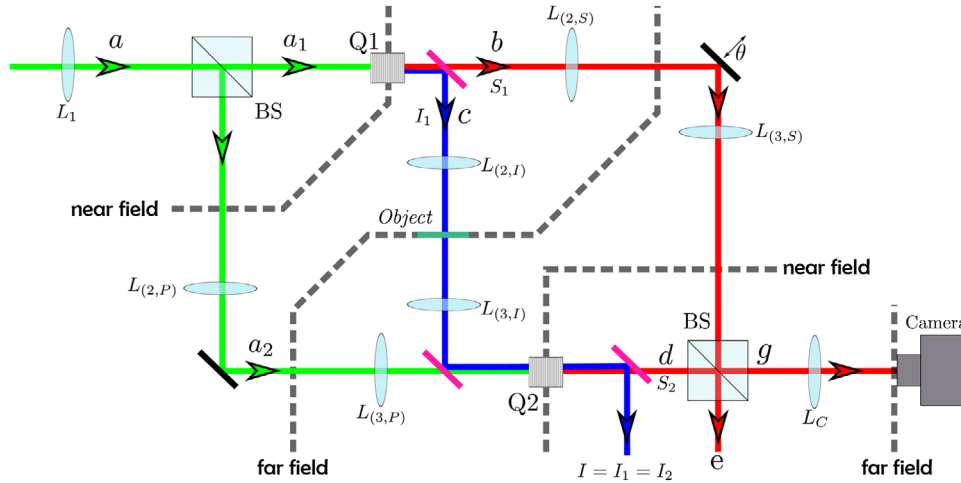
Figure 7. Quantum imaging with undetected light using momentum correlations. Pump beam, signal, and idler paths are denoted by green, blue, and red lines. QIUL is based on the induced coherence without induced emission effect in a spatially multimode scenario. In this case, the object and the camera are located at the far field plane of the crystals Q1 and Q2, respectively.

Therefore, one can consider a plane wave $\mathbf{k}_I$ of the idler photon emitted in Q1 and propagate it through the optical systems. The first lens the idler beam passes through performs a Fourier transform on it, generating the far field plane at the back focal plane of this lens. In other words, a plane wave $\mathbf{k}_I$ of the idler beam is converted into a spherical wave that is focused at a focal distance f_I to a point r_O in the object plane. Using the paraxial approximation, the representation of a point on the object is given by

$$\mathbf{r}_O \approx \frac{f_I \lambda_I}{2\pi} \mathbf{q}_I \tag{13}$$

where λ_I is the wavelength of the idler photon.

A second lens in the idler path at a distance f from the far field plane performs a second Fourier transform on the idler beam. The total operation of the first and second lenses in the idler path is a 4-f system, imaging the source plane Q1 onto the source plane Q2. If the impinging idler beam from Q1 ($\mathbf{q}_{I1}$) is perfectly aligned with the idler beam emitted at Q2 ($\mathbf{q}_{I2}$), then it can be assumed that $\mathbf{q}_{I1} = \mathbf{q}_{I2} = \mathbf{q}_I$. For a more precise theoretical description, see refs. [59, 63]. After this alignment, the idler photon
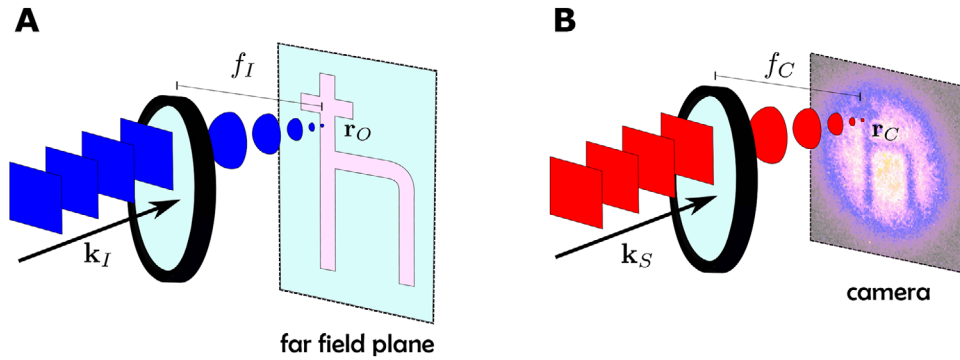
is discarded, and the total state changes to

$$|\psi\rangle = \frac{1}{\sqrt{2}} \int d\mathbf{q}_S \, d\mathbf{q}_I \, C(\mathbf{q}_I, \mathbf{q}_S) \, |\mathbf{q}_I\rangle \, (|\mathbf{q}_{S1}\rangle + e^{i\theta} |\mathbf{q}_{S2}\rangle) \tag{14}$$

3.3. Signal Photon Detection

Regarding signals emitted in Q1, these are 4-f imaged from their source plane onto a plane that "simulates" the source plane Q2. See the extension into the signal path b of the near field that passes through Q2 in Figure 7. Let us call this plane Q2-S1 for simplicity. From there, the signal beam impinges on a beam splitter (BS) where signal photons can be either transmitted or reflected with 50% probability. If the signal photon is reflected, it passes through a lens with a focal distance of f_C that performs a Fourier transform from the plane Q2-S1 to its back focal plane, where a camera is located to collect the signals. Thus, a plane wave $\mathbf{k}_{S1}$ is focused to a point $\mathbf{r}_C$ on the camera plane, meaning that a signal photon with transverse momentum $\hbar \mathbf{q}_{S1}$ is collected
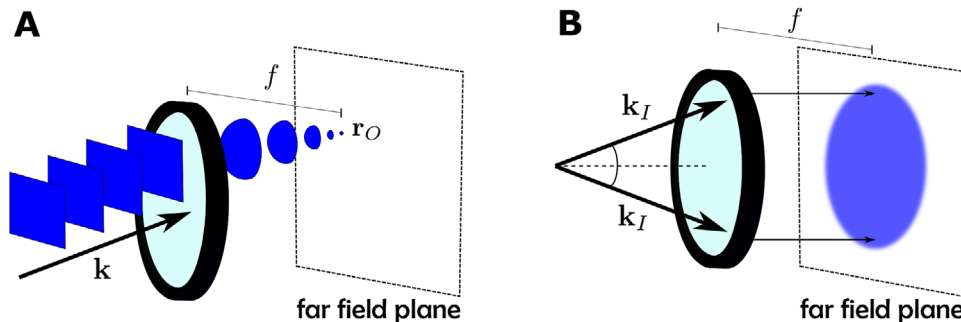
Figure 8. Plane wave decomposition and field-of-view formation. Let us consider how the field-of-view is formed by the idler beam. In the paraxial approximation, SPDC photons are emitted in small emission cones with respect to the optical axis. By Fourier decomposition, we can consider the SPDC beams as a sum of individual plane waves $\mathbf{k}_j$. A lens located in the idler path at a focal distance f from Q1, performs a Fourier transform on the idler photon forming the far-field plane at its back focal plane, i.e., the plane wave $\mathbf{k}_I$ is focused to a point $\mathbf{r}_O$ on the object. The field-of-view is formed in the far-field plane by considering the contribution of several idler plane waves in a collinear SPDC emission.[36]

2300353 (6 of 29)

**ADVANCED
SCIENCE NEWS**
www.advancedsciencenews.com

**ADVANCED
QUANTUM
TECHNOLOGIES**
www.advquantumtech.com

Figure 9. Object information transfer. Photon pairs emitted in a SPDC process are inherently correlated in space allowing to retrieve images with undetected photons. A) The object information is obtained by an idler photon with transverse momentum $\hbar\mathbf{q}_I$ passing through a point $\mathbf{r}_O$ on the object. B) The object information is retrieved by detecting a signal photon with transverse momentum $\hbar\mathbf{q}_S$ at a point $\mathbf{r}_C$ on the camera. This is possible due to $\mathbf{q}_I$ and $\mathbf{q}_S$ are related by $P(\mathbf{q}_I, \mathbf{q}_S)$.

at one pixel of the camera. The representation of $\mathbf{r}_C$ is

$$\mathbf{r}_C \approx \frac{f_C \lambda_S}{2\pi} \mathbf{q}_S \tag{15}$$

where λ_S is the wavelength of the signal photon.

In a similar way, the signal beam emitted in Q2 impinges on the same beam splitter but in its second input port, where again, the signal photon can be transmitted or reflected. The transmitted path of signal S2 coincides with the reflected path of signal S1, and consequently, the opposite is also true. Therefore, because of the lens in front of the camera, a plane wave $\mathbf{k}_{S2}$ transmitted through the BS is focused to a point $\mathbf{r}_C$ on the camera plane, wherein a signal photon with transverse momentum $\hbar\mathbf{q}_{S2}$ is detected.

Due to the alignment of idlers and recombination of signal beams, the which-source information is erased, and coherence is induced between the signal amplitudes. The signal photon intensity at one pixel of the camera is[35]

$$\langle N_S(\mathbf{r}_C) \rangle = \frac{1}{4} P_S(\mathbf{q}_S) \int d\mathbf{q}_I P(\mathbf{q}_I | \mathbf{q}_S) \{1 + \cos(\theta)\} \tag{16}$$

with $P(\mathbf{q}_I | \mathbf{q}_S) = P(\mathbf{q}_I, \mathbf{q}_S) / P_S(\mathbf{q}_S)$, and θ is a spatially invariant interferometric phase.

3.4. Object Information: From Idler to Signal

The object can have a structured complex transmission/reflection coefficient, $|R(\mathbf{r}_O)| e^{i\varphi_R(\mathbf{r}_O)}$. When the idler beam illuminates the object, each photon carrying a transverse momentum $\hbar\mathbf{q}_I$ can be absorbed/reflected or transmitted. Therefore, the object can be treated as a beam splitter in each one of its points $\mathbf{r}_O$.[59,63] Introducing the object in the idler path, Equation (17) changes to

$$\langle N_S(\mathbf{r}_C) \rangle \propto P_S(\mathbf{q}_S) \int d\mathbf{q}_I P(\mathbf{q}_I | \mathbf{q}_S) \{1 + |R(\mathbf{r}_O)| \cos(\varphi_R(\mathbf{r}_O) + \theta)\} \tag{17}$$

where the object information, phase (φ_R) and reflection/transmission ($|R|$), is contained in the interference pattern

of the signal photon. Moreover, the information of one point on the object $\mathbf{r}_O$ is related to the interference pattern modulation of one point on the camera $\mathbf{r}_C$. This object information transfer is depicted in **Figure 9**. In Figure 9A, an idler photon with transverse momentum $\hbar\mathbf{q}_I$ obtains the object information of a point $\mathbf{r}_O$ on the object. In Figure 9B, a signal photon with transverse momentum $\hbar\mathbf{q}_S$ is detected at a point $\mathbf{r}_C$ on the camera. Since the idler and signal photons are perfectly correlated through $P(\mathbf{q}_I, \mathbf{q}_S)$, the object information of a point $\mathbf{r}_O$ is extracted by a point on the camera $\mathbf{r}_C$. Considering many of these $\mathbf{q}$-vectors, it is possible to reconstruct a structured object, as was shown in the first implementation of this kind by G. B. Lemos et al. [12] in **Figure 10**.

3.4.1. Special Case: Uncorrelated Idler and Signal Photons

In the case that signal and idler particles are uncorrelated, the correlation function can be written as a separable state, i.e., $P(\mathbf{q}_I, \mathbf{q}_S) = P(\mathbf{q}_I) P(\mathbf{q}_S)$. Therefore, Equation (17) changes to[62]

$$\langle N_S(\mathbf{r}_C) \rangle \propto P_S(\mathbf{q}_S) \times \text{const.} \tag{18}$$

Thus no spatial information about the object is available in the signal photon intensity. Strictly speaking, this means that for *widefield* QIUL, one needs to have some degree of spatial correlations.
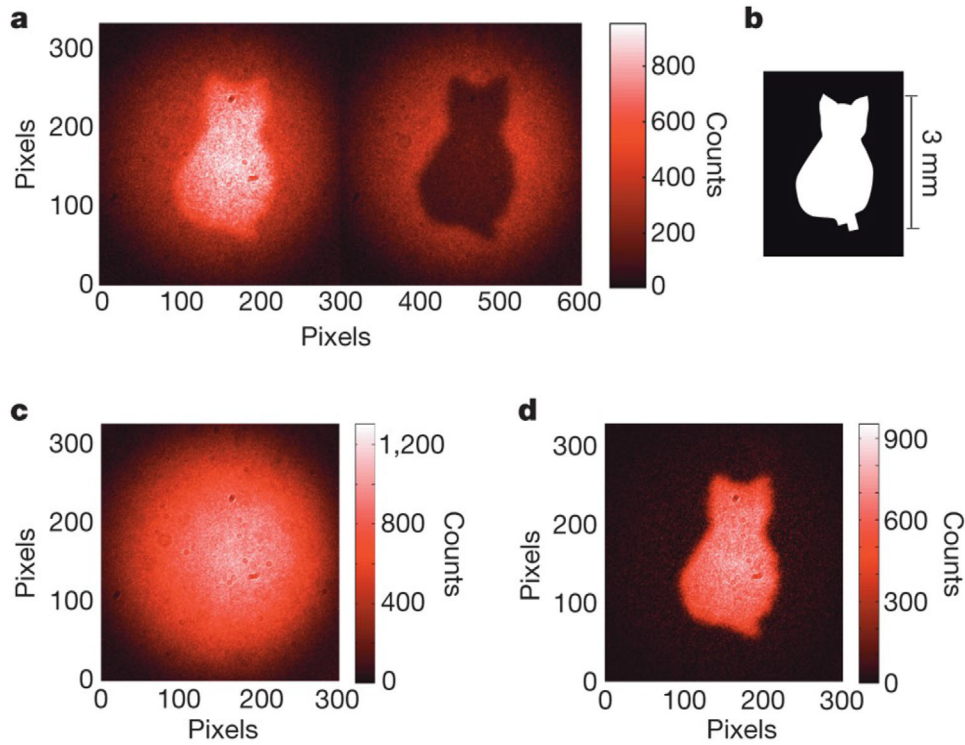
Nevertheless, it has been shown that induced coherence can be observed with separable states.[64] Therefore, the absence of spatial correlations will indicate that QIUL must be applied using a scanning approach.

3.5. Optical Magnification

The magnification in M-QIUL depends on the wavelengths of the photon pair and the lenses in the imaging system[12,59]

$$M = \frac{f_C \lambda_S}{f_I \lambda_I} \tag{19}$$

The magnification was experimentally tested in ref. [65], see **Figure 11**.

2300353 (7 of 29)

**ADVANCED
SCIENCE NEWS**

www.advancedsciencenews.com

**ADVANCED
QUANTUM
TECHNOLOGIES**

www.advquantumtech.com

Figure 10. Object and its image taken with undetected light. Reproduced with permission.[12] Copyright 2014, Springer Nature Limited.

$$\lambda_{I1} = 1550 \text{ nm}$$
$$\lambda_{S1} = 810 \text{ nm}$$

$$\lambda_{I2} = 780 \text{ nm}$$
$$\lambda_{S2} = 842 \text{ nm}$$
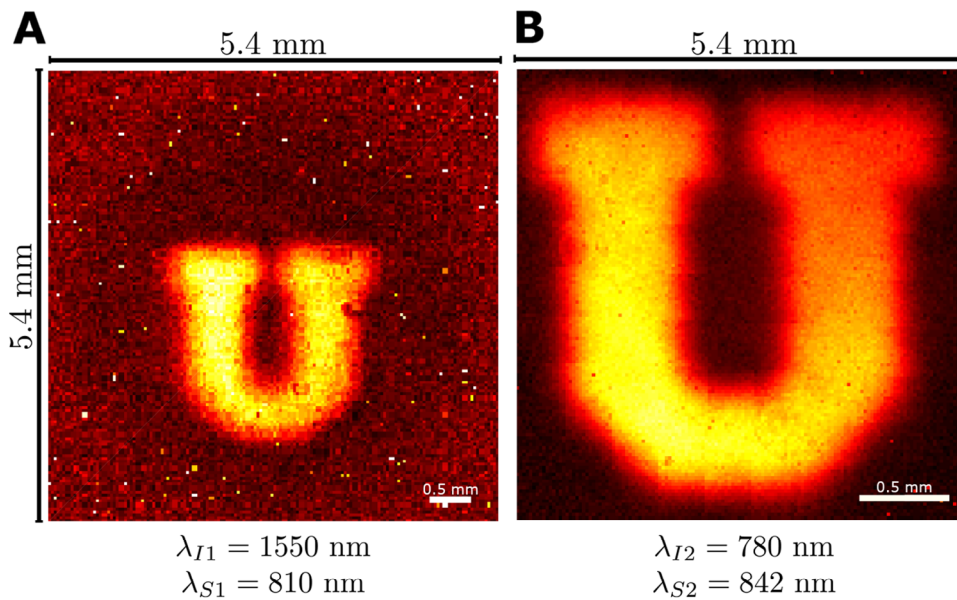
Figure 11. Magnification in M-QIUL. Figure 11 presents the magnification results for two experimental setups imaging the same object (2.417 mm × 2.3 mm). Setup 1 uses a set of wavelengths $\{\lambda_{I1} = 1550 \text{ nm}, \lambda_{S1} = 810 \text{ nm}\}$ and setup 2 uses $\{\lambda_{I2} = 742 \text{ nm}, \lambda_{S2} = 842 \text{ nm}\}$. In both setups the focal distances were preserved; $f_C = 150$ mm and $f_I = 75$ mm. In setup 1, it was obtained a magnification of $M_1 = 1.01 \pm 0.1$, which agrees with the theoretical expectation of 1.045. In setup 2, the resulting experimental magnification was $M_2 = 2.16 \pm 0.1$, also agreeing with its prediction of 2.16. Image adapted from.[65]
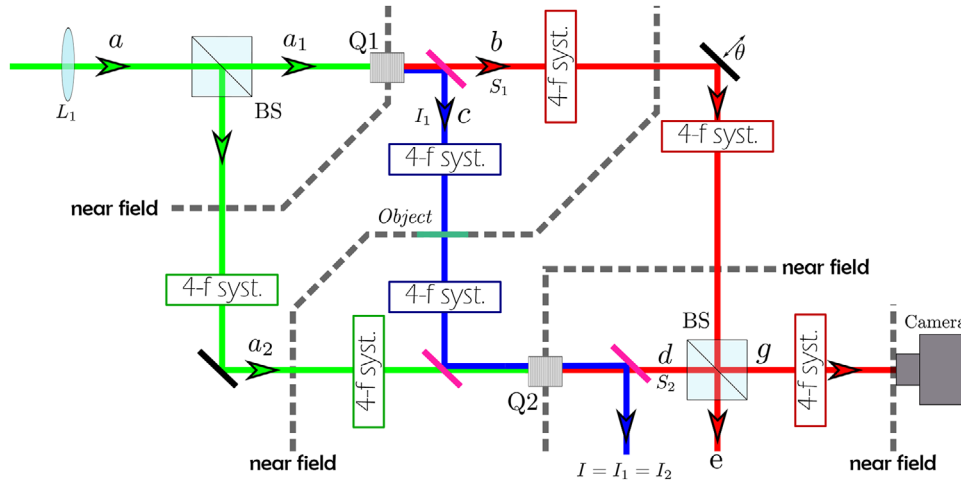
Figure 12. Quantum imaging with undetected light using position correlations. Pump beam, signal, and idler paths are denoted by green, blue, and red lines. QIUL can also be performed by employing position correlations. For this, the object and the camera are images of the crystals Q1 and Q2 (near field planes), respectively.

4. QIUL Based on Position Correlations

Quantum imaging usually employs photon pairs spatially correlated in two planes: far field and near field.[31,66,67] The far field plane was analyzed in the previous section and shows how photon pairs are anticorrelated in momentum. In the near field plane, photon pairs are "position correlated," which can also be employed to perform QIUL. Position based QIUL (P-QIUL) was theoretically introduced in ref. [68] and experimentally realized in refs. [69, 70]. Here we review the main features of P-QIUL and its differences from M-QIUL.

4.1. Imaging System

Position correlation comes from the position birth of a photon pair inside a nonlinear medium. Let us consider that, in the source plane, the signal and idler photons have transverse positions ρ_S and ρ_I, respectively. In this imaging technique, sketched in **Figure 12**, a 4-f system on the idler path is performed to image the source plane onto the object plane. The 4-f system produces a magnification M_I from the source into the object. Thus a point in the object ρ_O is related to a point in the source ρ_I by

$$\rho_O = M_I \rho_I \tag{20}$$

Hence, the field-of-view is directly connected to the pump beam waist w_P inside the nonlinear medium and to the magnification M_I.[69] Note that in P-QIUL, the field-of-view is not obtained by the Fourier decomposition of **k**-vectors as in M-QIUL but from the convolution of many points $\{\rho_I\}$.[68] After acquiring the object information, the idler photon is 4-f imaged onto the source plane Q2. In a similar way to the momentum case, this finalizes the alignment of the idlers.

In the case of signal beams emitted in both sources, these are recombined with a BS and collected by a camera. However, the optical elements in their paths to the camera differ. The signal photon emitted in Q2 (Q1) is imaged on the camera plane with one (two) 4-f system(s). Considering that the 4-f system produces

a total magnification of M_S, then a point on the camera ρ_C is related to a point on the source ρ_S by

$$\rho_C = M_S \rho_S \tag{21}$$

On the camera, the signal photon intensity is given by[68]

$$\langle N_S(\rho_C) \rangle \propto \int d\rho_I P(\rho_I, \rho_S)\{1 + |R(\rho_O)| \cos(\varphi_R(\rho_O) + \theta)\} \tag{22}$$

where an object, with a complex transmission amplitude of $|R(\rho_O)|e^{i\varphi_R(\rho_O)}$, is located at the image plane of the source Q1. And where the form of the two-photon joint probability density is given by

$$P(\rho_I, \rho_S) \propto \left| \int d\mathbf{q}_I \, d\mathbf{q}_S \, C(\mathbf{q}_I, \mathbf{q}_S) \exp\{i(\mathbf{q}_I \cdot \rho_I + \mathbf{q}_S \cdot \rho_S)\} \right|^2 \tag{23}$$

4.2. Differences between Position and Momentum Imaging with Undetected Light

There are three main differences between these two types of images: magnification, correlations, and resolution. In M-QIUL, the former has a dependence given in Equation (19). However, in P-QIUL, the total magnification depends on the magnifications performed by the 4-f systems on signal and idler paths. The total magnification in P-QIUL is[68]

$$M_T = \frac{M_S}{M_I} \tag{24}$$

The second difference, as one can already have noticed, is the spatial correlations employed in acquiring and reconstructing the image. While in position the two photons are correlated in space; in momentum, the two photons are anticorrelated. Depending on the type of correlation, these are enhanced by different parameters, e.g., the pump waist in M-QIUL and the crystal length in P-QIUL.

**ADVANCED
SCIENCE NEWS**

www.advancedsciencenews.com

**ADVANCED
QUANTUM
TECHNOLOGIES**

www.advquantumtech.com

Finally, the differences in resolution are exposed in section 5.

In practical terms, P-QIUL might have some advantages with respect to the momentum counterpart. For example, P-QIUL could be implemented with cheap lasers carrying poor coherence without diminishing spatial resolution. The opposite occurs with momentum correlations.[71,72] Therefore, in principle, P-QIUL might require less expensive components to be assembled.

5. Spatial Resolution of QIUL

The resolution of QIUL is not a trivial problem since it involves a photon pair with different wavelengths and several parameters in the generation of this pair. Therefore, before the first experimental implementation, several hypotheses about the parameters governing its resolution were present in the community, such as

a) the longest wavelength
b) the idler wavelength
c) the signal wavelength
d) a combination of both photons' wavelengths

Surprisingly, many of these initial hypotheses are correct, but of course, not all of them simultaneously. The reason is parameters governing the spatial resolution of QIUL change depending on the approximations, which are settled by experimental conditions. Here, we present in which regimes these hypotheses are valid.

5.1. Thin Crystal Approximation

In 1998, C. H. Monken et al. introduced the thin crystal approximation.[73] This approximation is within the paraxial regime, where the emission angle of the photon pair emitted in an SPDC process is small. If the crystal length L_z is small in comparison to $|\mathbf{q}_I|^{-1}$ and $|\mathbf{q}_S|^{-1}$, then the joint amplitude density can be approximated to the angular spectrum of the pump beam

$$C(\mathbf{q}_I, \mathbf{q}_S) \propto \mathscr{A}(|\mathbf{q}_P|^2) = \mathscr{A}(|\mathbf{q}_I + \mathbf{q}_S|^2) \quad (25)$$

The first article studying the resolution of M-QIUL[65] works under this approximation and answers the questions of wavelength and momentum correlation dependency.

5.1.1. Momentum Correlation Dependency

From hereon, we consider a more realistic model of correlations in our imaging system, i.e., an imperfect momentum correlation case, $P(\mathbf{q}_I|\mathbf{q}_S) \neq \delta(\mathbf{q}_I + \mathbf{q}_S)$. Considering a pump beam with a Gaussian distribution, i.e., $\mathscr{A} \propto \exp\left(-|\mathbf{q}_I + \mathbf{q}_S|^2 w_P^2/4\right)$, where w_P is its pump waist, then

$$P(\mathbf{q}_I|\mathbf{q}_S) \propto \exp\left(\frac{-|\mathbf{q}_I + \mathbf{q}_S|^2 w_P^2}{2}\right) \quad (26)$$

Equation (26) indicates that the momentum correlation between signal and idler photons is determined by the size of the
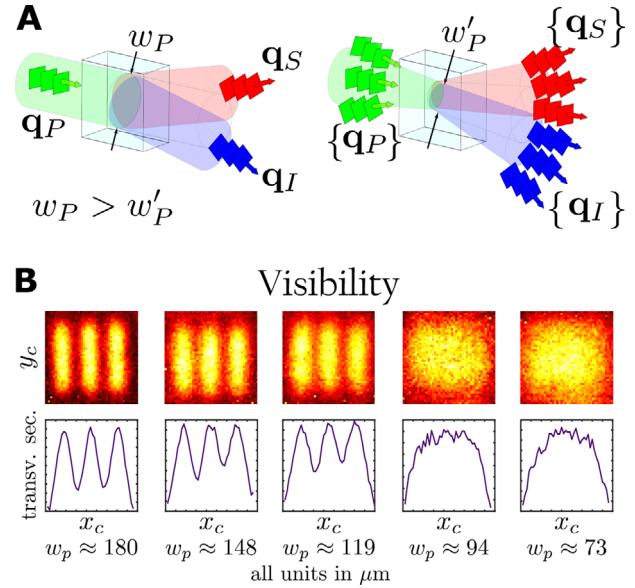
Figure 13. Qualitative results: Momentum correlation. Reproduced with permission.[65]

pump waist into the crystal. Thus by detecting one signal photon with a transverse momentum $\hbar\mathbf{q}_S$, its idler photon partner can be found in a range of different transverse momenta $\{\hbar\mathbf{q}_I\}$ determined by the size of the pump waist w_P. Before we analyze the consequences of w_P in the resolution, note that here the diffraction effects are neglected. This does not mean that diffraction does not contribute to the resolution of the obtained images, just that its contribution is very small in comparison to the momentum correlation.

Without loss of generality, let us consider a pure transmissive/reflective object (i.e., amplitude object with $\varphi_R = 0$). The object information of a transmissive/reflective object is contained in the signal photon visibility. From Equation (17), the corresponding visibility at a point $\mathbf{r}_C$ on the camera is given by[65]

$$\mathcal{V}_S(\mathbf{r}_C) = \int d\mathbf{q}_I \, P(\mathbf{q}_I|\mathbf{q}_S) \, |R(\mathbf{r}_O)| \quad (27)$$

By considering many points on the camera, a "visibility image" is obtained. The experimental results presented below correspond to transmissive objects. However, phase objects follow the same behavior as shown in ref. [65].

Figure 13 shows qualitative results of the momentum correlation. It is shown that a bigger pump waist enhances the image resolution of a three slit object, with signal wavelength λ_S = 810 nm and idler wavelength λ_I = 1550 nm. The explanation of this can be visualized in **Figure 14**. Since the object has a structured shape, it needs to be illuminated by an idler beam. An idler photon "1" with a transverse momentum $\hbar\mathbf{q}_{I1}$ passes through a point on the object $\mathbf{r}_{O1}$. Likewise, a second idler photon "2" with a transverse momentum $\hbar\mathbf{q}_{I2}$ passes through a point on the object $\mathbf{r}_{O2}$, and so on and so forth. In this way, the object information of $\{\mathbf{r}_O\}$ points is carried by $\{\hbar\mathbf{q}_I\}$ transverse momenta. Since one signal transverse momentum $\hbar\mathbf{q}_S$ is related to a set of transverse momenta $\{\hbar\mathbf{q}_I\}$ by $P(\mathbf{q}_I|\mathbf{q}_S)$, one point on the
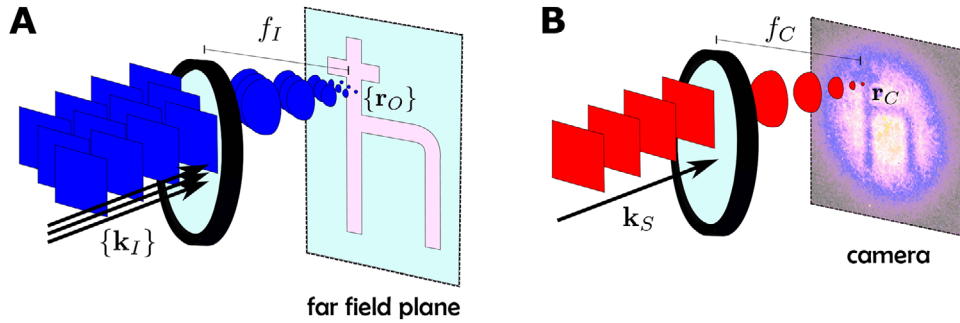
**ADVANCED
SCIENCE NEWS**
www.advancedsciencenews.com

**ADVANCED
QUANTUM
TECHNOLOGIES**
www.advquantumtech.com

Figure 14. Effects of momentum correlation on resolution.

camera $\mathbf{r}_C$ receives the contribution of several points on the object $\{\mathbf{r}_O\}$. This is how the resolution of M-QIUL relies on "how many points on the object $\{\mathbf{r}_O\}$ are transferred to one point on the camera $\mathbf{r}_C$," where the relation between $\{\mathbf{r}_O\}$ and $\mathbf{r}_C$ is governed by $P(\mathbf{q}_I|\mathbf{q}_S)$. Therefore, from Equation (26), the resolution of M-QIUL is directly connected to w_P. Furthermore, these qualitative results are in agreement with other works analyzing the resolution of quantum imaging techniques based on bulk crystals, e.g., ghost imaging.[58]

5.1.2. Wavelength Dependency

Reference [65] also presents quantitative results. This further analysis helps to understand the role of the wavelengths in M-QIUL.

Consider a knife-edge object along the y-axis on the object plane. This object can be modeled with a Heaviside step function, $|R(\mathbf{r}_O)| = R(x_O, y_O) = 0$ for $x_O < x'_O$ and $R(x_O, y_O) = 1$ for $x_O \geq x'_O$. Using Equation (27), we get the visibility image for a knife-edge object

$$\mathcal{V}_S(\mathbf{r}_C) \propto 1 - \mathrm{erf}\left(\frac{x_O - M x'_O}{\sigma_C}\right) \tag{28}$$

where erf is an error function, σ_C is its characteristic spread (see **Figure 15**), and M is the magnification given in Equation (19).

The spread on the camera σ_C is given by

$$\sigma_C = \frac{f_C \lambda_S}{\sqrt{2}\pi w_P} \tag{29}$$

From Equation (29), it can be noted that σ_C depends only on the signal photon detected on the camera. Since the value of σ_C can usually be associated with the resolution of an optical system,[74] this would mean that the resolution depends exclusively on the signal photon. However, in this case, the spread on the camera σ_C is not directly connected to the resolution and needs to be corrected by the magnification M of the system.[75] By doing this, the spread σ associated with the resolution is

$$\sigma = \frac{\sigma_C}{M} = \frac{f_C \lambda_S}{\sqrt{2}\pi w_P} \times \frac{f_I \lambda_I}{f_C \lambda_S} = \frac{f_I \lambda_I}{\sqrt{2}\pi w_P} \tag{30}$$

Ultimately meaning that the resolution is given exclusively by the idler wavelength, which is the photon that illuminates the object.

The above conclusions were tested with two experimental realizations,[65] each of which with a different phase-matching condition but similar experimental characteristics, such as optical components, crystal dimensions, and optical distances. In setup 1, a pump beam of $\lambda_{P1} = 532$ nm was used to generate
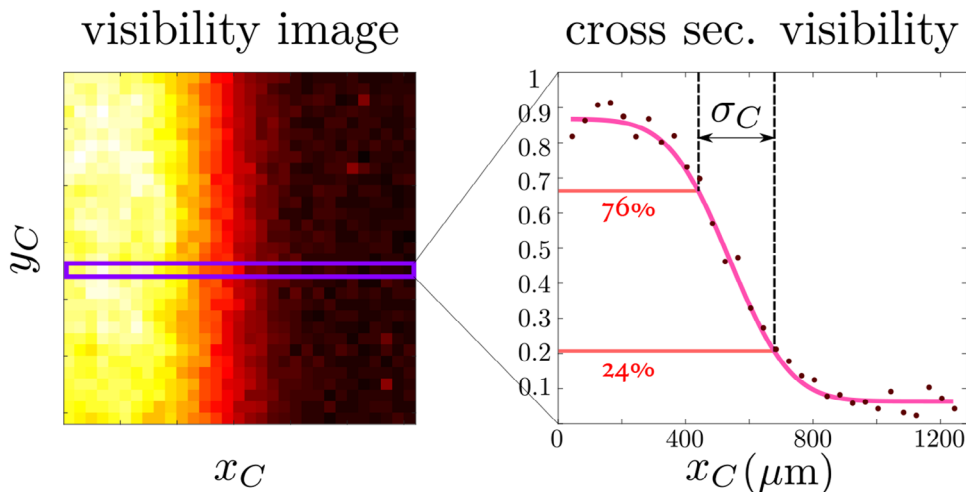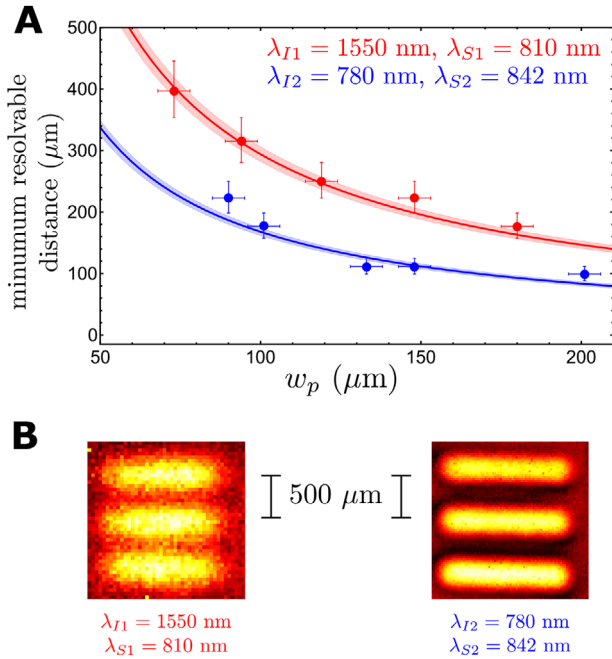

Figure 15. Image of a knife-edge object. Reproduced with permission.[65]

**ADVANCED
SCIENCE NEWS**

www.advancedsciencenews.com

**ADVANCED
QUANTUM
TECHNOLOGIES**

www.advquantumtech.com

Figure 16. Experimental results for the resolution of M-QIUL in the thin crystal approximation. Reproduced with permission.[65]

a signal $\lambda_{S1} = 810$ nm and an idler $\lambda_{I1} = 1550$ nm. In setup 2, a pump beam of $\lambda_{P2} = 405$ nm was used to generate a signal $\lambda_{S2} = 842$ nm and an idler $\lambda_{I2} = 780$ nm. As we can note from the phase-matching conditions, signal photons have similar wavelengths, whereas idler photons have very different ones. Now if Equation (30) is correct, then, the images obtained by setup 2 should show a better resolution than the images obtained by setup 1. **Figure 16** shows the experimental images of a two-slits object obtained by setups 1 and 2. Figure 16A presents the minimum resolvable distance $\mathcal{R}$ of a two-slit object, which was adapted from the Rayleigh criterion.[76] Solid lines correspond to theoretical predictions, data points correspond to experimental results, and red and blue colors correspond to setups 1 and 2, respectively. $\mathcal{R}$ is calculated considering the two visibility maxima and the visibility minima between these two picks, such $\mathcal{R} = \mathcal{V}_{\min}/(\mathcal{V}_{\max1} + \mathcal{V}_{\max2})$. From the Rayleigh criterion, if $\mathcal{R} \leq 0.81$, the two slits are so-called "resolvable." In Figure 16A, it is clear that the resolution increases with i) a bigger w_P and ii) a shorter wavelength of the idler photon. Figure 16B shows two images of the same object taken with the same pump waist in setups 1 (left) and 2 (right). Evidently, the image that was acquired with the shortest idler wavelength shows a higher resolution (setup 2). In conclusion, in the thin crystal approximation, the resolution of M-QIUL is determined by the photon wavelength that illuminates the object.

5.1.3. How to Increase the Spatial Resolution: Microscopy with Undetected Light

From Equation (30), few parameters can be optimized to reduce the spread σ and, therefore, enhance the resolution. The first option is reducing the wavelength of the idler photon that illumi-

nates the object. Alternatively, the pump waist at the crystal(s) can be increased. Lastly, the same effect is achieved by reducing the focal length of the lens in the idler path. In this case, the resolution increases at the expense of reducing the field of view. Doing the latter in a ZWM interferometer is not an easy task due to obvious reasons. However, this becomes a natural approach in an SU(1,1) interferometer. In refs. [19, 20, 77, 78], M-QIUL were implemented using a SU(1,1) interferometer. In ref. [20], it is also experimentally showed how to enhance the resolution by reducing the field-of-view, see **Figure 17**. Their experimental results are shown in Figure 17 (right). The reduction of the field-of-view can be compensated by performing a scanning approach; in this way, it is simultaneously obtained an optimal field-of-view and a high resolution.

In recent years, M-QIUL has also been optimized in different experimental aspects such as acquisition speed,[18] loss compensation,[79] and reducing its size and price.[80]

5.1.4. Thin Crystal in P-QIUP

Within the thin crystal approximation, the resolution of P-QIUL has been theoretically investigated in ref. [81] and experimentally corroborated in ref. [70]. In this regime, the term containing the pump waist w_P can be considered as a constant compared to the term containing the crystal length. Note that this is only valid for big pump waists[70] i.e., for pump waists fulfilling the conditions: $w_P^2 \gg \lambda_S^2 L_z/(\lambda_S + \lambda_I)$ and $w_P^2 \gg \lambda_I^2 L_z/(\lambda_S + \lambda_I)$. Hence, the joint probability density is approximated to
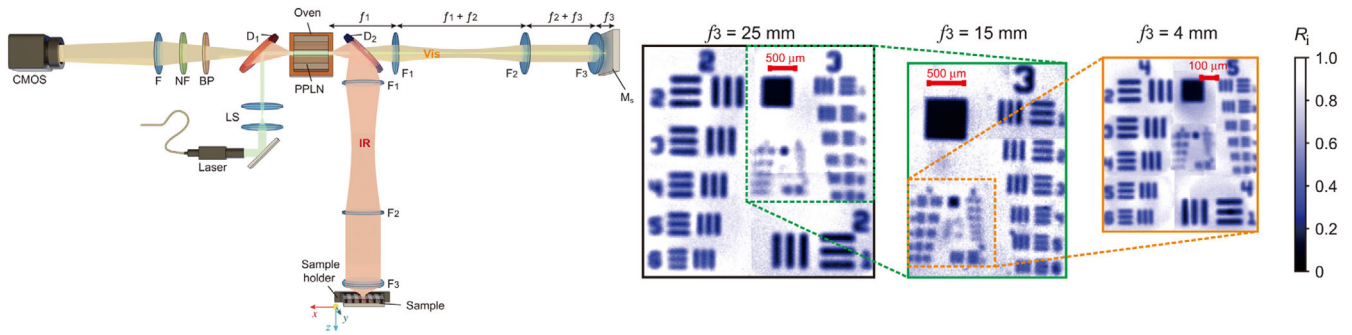
$$P(\boldsymbol{\rho}_I, \boldsymbol{\rho}_S) = P\left(\frac{\boldsymbol{\rho}_O}{M_I}, \frac{\boldsymbol{\rho}_C}{M_S}\right) \propto \text{const.}$$

$$\times \exp\left[-\frac{4\pi}{L_z(\lambda_I + \lambda_S)}\left|\frac{\boldsymbol{\rho}_C}{M_S} - \frac{\boldsymbol{\rho}_O}{M_I}\right|^2\right] \quad (31)$$

where the sinc function was approximated to a Gaussian function. From Equation (31), it was calculated the spread of a point spread function (PSF), which similar to the spread of an edge spread function, is related to the resolution of the optical system. This spread σ_{PSF} linked to the resolution of P-QIUL is

$$\sigma_{\text{PSF}} = \frac{M_I}{2\sqrt{\pi}}\sqrt{L_z(\lambda_S + \lambda_I)} \quad (32)$$

Therefore, σ_{PSF}, and consequently, the resolution, is proportional to the crystal length and *both* photons wavelengths. This brings two important differences between momentum- and position-based QIUL. First, the crystal length is the main factor in the resolution of P-QIUL instead of w_P. Second, both photons' wavelengths are equally important on the resolution of P-QIUL instead of just being the photon illuminating the object.

Experimentally, the resolution of P-QIUL was tested by changing the crystal length and the pump waist, see **Figure 18**. The theory developed by Viswanathan is included as dotted lines for different crystal lengths, see inset. For a fixed set of wavelengths (idler = 910 nm; signal = 730 nm), the experimental results show that a higher resolution is obtained with shorter crystals. The results also matched the theory presented in ref. [81] for big pump

ADVANCED
SCIENCE NEWS
www.advancedsciencenews.com

ADVANCED
QUANTUM
TECHNOLOGIES
www.advquantumtech.com

Figure 17. Enhancing resolution at the expense of the field of view. (Left) M-QIUL implemented in an SU(1,1) interferometer. (Right) Spatial resolution enhancement was obtained by replacing the lens in front of the object with f = 25, 15, and 4 mm. Reproduced with permission.[20] Copyright 2022, American Association for the Advancement of Science.
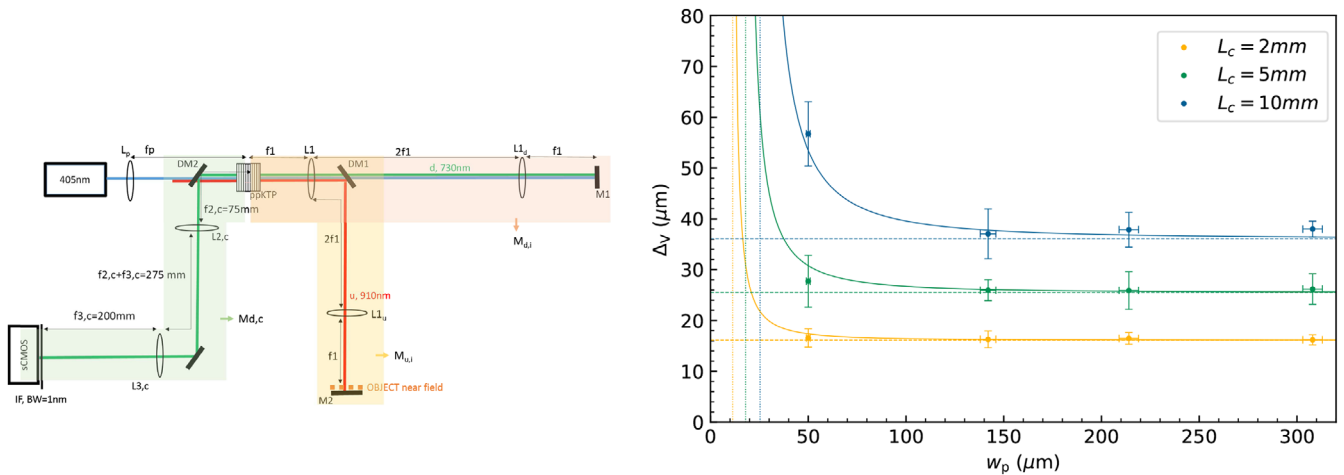
Figure 18. Experimental resolution in P-QIUL. (Left) P-QIUL implemented in an SU(1,1) interferometer. (Right) Spatial resolution results for different crystal lengths of L = 2, 5, and 10 mm. Reproduced with permission.[70] Copyright 2023, American Physical Society.

waists. However, for small pump waist, theory and experiment start to differ. This is because the bi-photon state starts to lose spatial correlations for small pump waists, ending up in a separable state. A more precise theory, including the effects of small pump waists, can be found in ref. [70].

5.2. Beyond the Thin Crystal Approximation: Ultra-Thin and Thick Crystals

In the paraxial regime, the thin crystal approximation is currently the most applicable range of QIUL. Beyond thin crystals, there are two other regimes: thick crystals and ultra-thin crystals. The former, albeit increasing the photon pair efficiency, also reduces the spatial resolution and is more suitable in other quantum technological applications such as quantum communications. The latter is essential to increase the spatial resolution and helps to understand the resolution limits of many quantum imaging techniques based on photon pairs, QIUL and GI included.
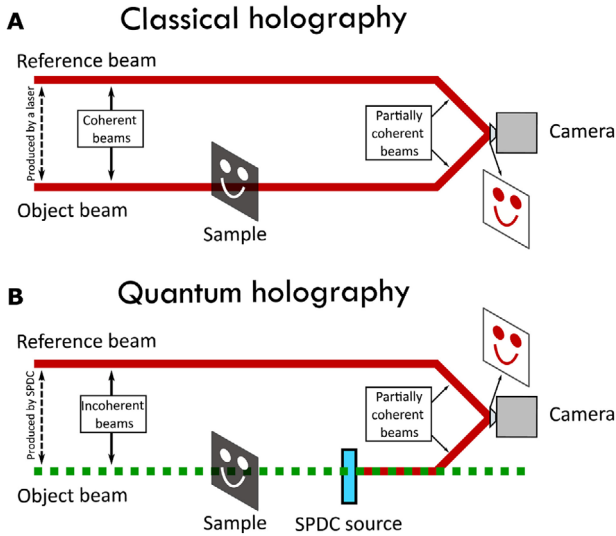
Ultra-thin crystals have the characteristic that their lengths are in the order of the SPDC photons' wavelengths.[82] Thus, the localization of a photon pair emission is extremely precise, and the range of momenta of those photons is much broader, such that a non-paraxial regime analysis is required. In the following, we

resume the main parameters determining the resolution in the non-paraxial regime introduced by A. Vega et al.[63]

When the crystal length L_z starts decreasing, the photon pair emission angle opens up depending on its wavelengths, λ_S and λ_I, reaching a maximum of 90°. Considering a pump waist composed of one plane wave, there are two different resolution limits for the wavelengths, which are depicted in **Figure 19**. The
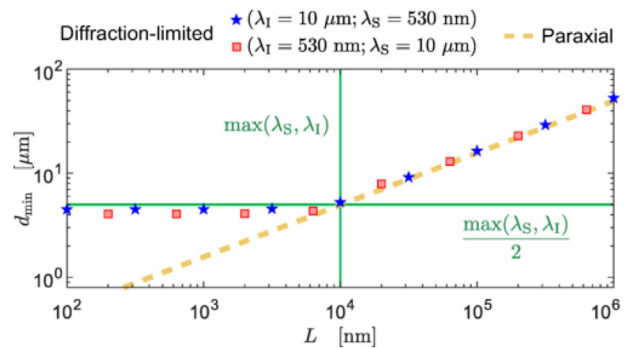
Figure 19. From paraxial to diffraction-limited resolution. Reproduced with permission.[63] Copyright 2022, American Physical Society.

**ADVANCED
SCIENCE NEWS**

www.advancedsciencenews.com

**ADVANCED
QUANTUM
TECHNOLOGIES**

www.advquantumtech.com

Figure 20. Classical holography and quantum holography with undetected light. Reproduced with permission.[26] Copyright 2022, American Association for the Advancement of Science.

resolution was obtained by analysing a two-slits object separated by a distance d. The minimum resolvable distance, d_{min}, corresponds to the ratio between minimum and maximum visibilities equal to $\mathcal{R} = 0.80$. When the crystal length is longer than both SPDC photons' wavelengths, the resolution is limited by the longest wavelength $\max(\lambda_S, \lambda_I)$. Once the crystal length gets shorter than the longest SPDC wavelengths, the resolution reaches the diffraction limit and, therefore, is limited by $\max(\lambda_S, \lambda_I)/2$. If one considers a realistic pump waist, the authors found out that the limiting resolution is slightly different to $\max(\lambda_S, \lambda_I)/2$ and that the pump waist does not affect this limit; more details in ref. [63]. It is noteworthy to emphasize that Vega's work introduced the two-photon equivalence of the classical diffraction limit.

On the other extreme, we have thick crystals. In this case, one then has to take into account the contribution of both functions depending on the pump waist and crystal length. Resolution in thick crystals was numerically analyzed in ref. [63] and analytically realized in ref. [70]. By considering both parameters, pump waist and crystal length, spatial resolution is rapidly diminished; more details in ref. [70].

6. Quantum Holography

In 1948, D. Gabor introduced the principles of optical holography in his paper *A New Microscopic Principle*.[83] This discovery awarded Gabor the Nobel Prize in Physics. Holography has been applied in the classical[84,85] as well in the quantum domains,[86,87] with applications ranging from retrieving the spatial structure of single photons to biomedical microscopy to monitor neural activity.

Holography is a technique that retrieves the object information, phase and amplitude, by means of the interference of two optical fields. One of these fields interacts with the object, and the remaining field is employed as a reference, see **Figure** 20A. In this section, we review two holography works in the quantum

domain using undetected light, i.e., the probing beam remains undetected, see Figure 20B.

6.1. Quantum Holography with Undetected Light

Quantum holography with undetected light (QHUL),[26,88,89] is the first implementation of this kind, and it is inspired by *phase-shifting digital holography* (PSDH), introduced by I. Yamaguchi and T. Zhang.[90] In QHUL, the optical path of the idler photon is varied which we henceforth refer to as *steps* of a *QHUL algorithm*. With this, the relative phase θ between signal and idler photons is changed and, therefore, a set of different interference patterns is obtained. From Equation 17, we have that the signal photon intensity at one pixel of the camera is

$$\langle N_S \rangle_{\theta_m} \propto \{1 + |R(\mathbf{r}_O)| \cos(\varphi_R(\mathbf{r}_O) + \theta_m)\}. \tag{33}$$

To exemplify the object information retrieval by QHUL, let us consider its four-step algorithm, i.e., $\theta_4 = 0, \pi/2, \pi$, and $3\pi/2$. The signal photon intensity for these four values are

$$\langle N_S \rangle_0 \propto 1 + |R(\mathbf{r}_O)| \cos(\varphi_R(\mathbf{r}_O)) \tag{34}$$

$$\langle N_S \rangle_{\pi/2} \propto 1 - |R(\mathbf{r}_O)| \sin(\varphi_R(\mathbf{r}_O)) \tag{35}$$

$$\langle N_S \rangle_\pi \propto 1 - |R(\mathbf{r}_O)| \cos(\varphi_R(\mathbf{r}_O)) \tag{36}$$

$$\langle N_S \rangle_{3\pi/2} \propto 1 + |R(\mathbf{r}_O)| \sin(\varphi_R(\mathbf{r}_O)) \tag{37}$$

Considering Equations (34)–(37), then the object information is obtained by

$$|R(\mathbf{r}_O)| = 2 \times \frac{\left(\left[\langle N_S \rangle_{3\pi/2} - \langle N_S \rangle_{\pi/2} \right]^2 + \left[\langle N_S \rangle_0 - \langle N_S \rangle_\pi \right]^2 \right)^{1/2}}{\langle N_S \rangle_0 + \langle N_S \rangle_{\pi/2} + \langle N_S \rangle_\pi + \langle N_S \rangle_{3\pi/2}} \tag{38}$$
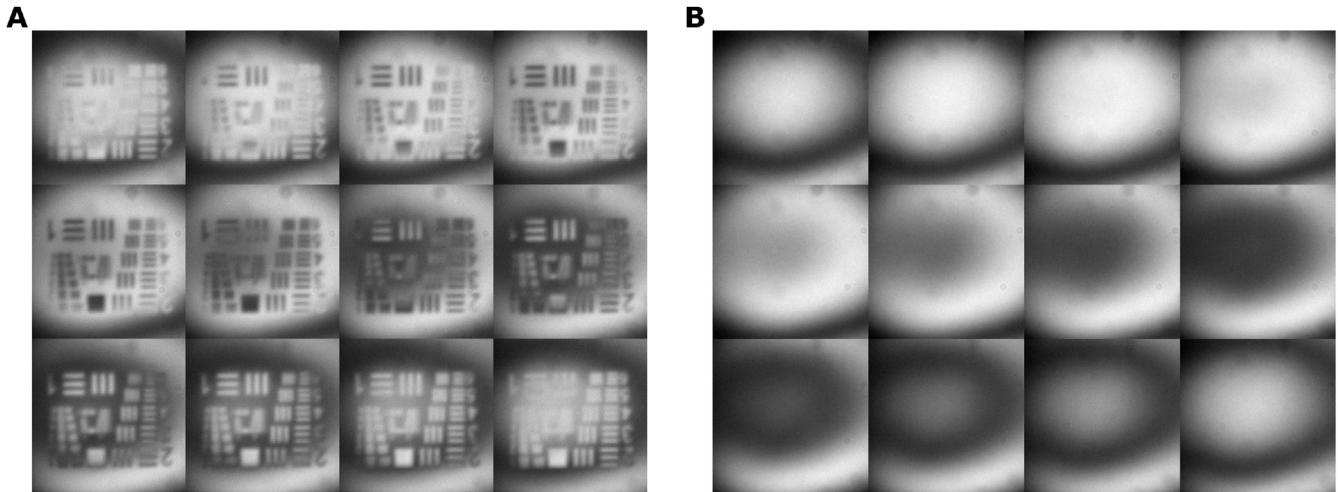
$$\varphi_R(\mathbf{r}_O) = \arctan\left(\frac{\langle N_S \rangle_{3\pi/2} - \langle N_S \rangle_{\pi/2}}{\langle N_S \rangle_0 - \langle N_S \rangle_\pi} \right) \tag{39}$$

QHUL can also be implemented with different numbers of steps, with a minimum of three. **Figure** 21 shows a QHUL of 12 steps. In general, for M-steps, the transmission and phase can be retrieved by

$$|R(\mathbf{r}_O)| = 2 \times \frac{\left\{ \left[\sum_m \langle N_S \rangle_{\theta_m} \cos(\theta_m) \right]^2 + \left[\sum_m \langle N_S \rangle_{\theta_m} \sin(\theta_m) \right]^2 \right\}^{1/2}}{\sum_m \langle N_S \rangle_{\theta_m}} \tag{40}$$

$$\varphi_R(\mathbf{r}_O) = -\arctan\left[\frac{\sum_m \langle N_S \rangle_{\theta_m} \sin(\theta_m)}{\sum_m \langle N_S \rangle_{\theta_m} \cos(\theta_m)} \right] \tag{41}$$

with $\theta_m = 2m\pi/M$, and $m = 0 \ldots M - 1$. A detailed derivation of Equations (40) and (41) are presented in ref. [26].

ADVANCED
SCIENCE NEWS

www.advancedsciencenews.com

ADVANCED
QUANTUM
TECHNOLOGIES

www.advquantumtech.com

A

B

Figure 21. 12-step QHUL. Here is presented a 12-step QHUL procedure, where every image corresponds to one step of the algorithm. On the left, there are images scattered by the object of interest, and on the right, there are images of the reference beam. The light that illuminated the object remains undetected. Reproduced with permission.[26] Copyright 2022, American Association for the Advancement of Science.

Intuitively, one can imagine that the performance varies depending on the QHUL algorithm. **Figure 22** presents the experimental results of QHUL varying the number of steps and the detection window time. The results show that for a higher number of steps in QHUL, a higher phase accuracy of the image is retrieved. Similarly, by increasing the detection time, the image phase accuracy is also increased. We will expand these results on phase accuracy in section 6.2.

6.2. Quantum Imaging Distillation

Quantum imaging offers several advantages and fascinating properties over classical imaging. One example is "imaging distillation" that separates a quantum image from an environment with which this image has interacted.[91–93] Similar techniques have been applied to quantum cryptography to, for example, increase the distance of a quantum link.[94] Quantum imaging distillation uses quantum correlations of photon pairs and has been implemented with different degrees of freedom, such as spatial correlations,[95,96] time correlations,[97] frequency-time correlations,[98] and spatio-temporal correlations.[99] All these distillation techniques have been applied using a joint detection of photon pairs. Here, we introduce an imaging distillation technique based on QHUL, i.e., employing single-photon detection.[28]

6.2.1. Distillation Principle

Let us consider two images to introduce distillation imaging with undetected light, see **Figure 23**. The first one is the quantum image of interest, depicted in Figure 23a (right). The second one is a classical image representing noise in Figure 23b (right). The superposition of these two images is shown in Figure 23c (right). Figure 23d (right) presents the resulting distilled image.

6.2.2. Distillation Results

Consider a noise intensity $\langle N_T \rangle$ with a variance $\langle (\Delta N_T)^2 \rangle$ being collected by the camera; see Figure 23 (left). In ref. [28], it is shown that the variance of a phase object $\langle (\Delta \varphi_R)^2 \rangle$ extracted by QHUL and affected by an external source of noise corresponds to
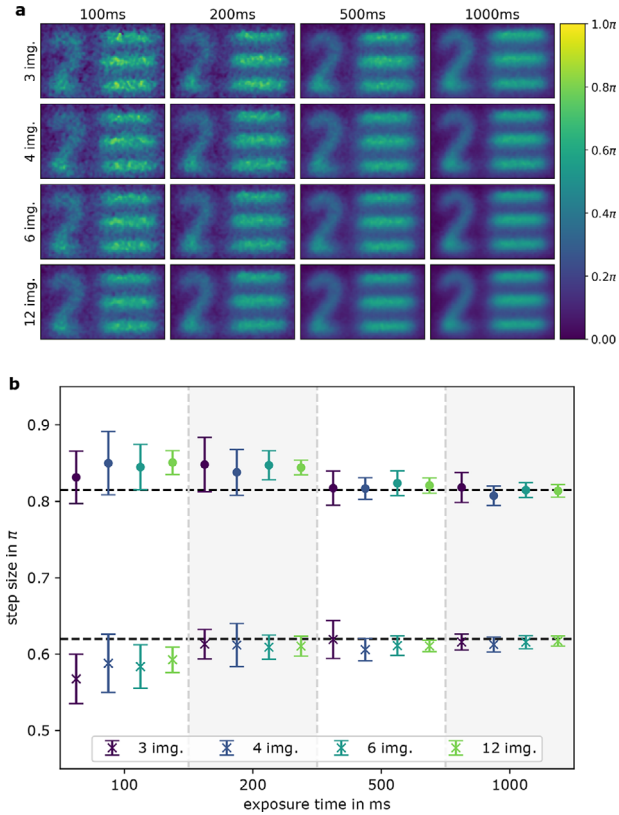
$$\langle (\Delta \varphi_R)^2 \rangle = \frac{1}{M \, \mathcal{V}_S^2 \, S_0} \left[1 + \frac{\langle (\Delta N_T)^2 \rangle}{2 \, S_0} \right] \tag{42}$$

S_0 is the number of idler photons illuminating the object, M is the number of steps in QHUL, and $\mathcal{V}_S$ is the signal photon visibility. The phase variance has two main contributions. First, the QHUL algorithm and the experimental conditions, including the SPDC process, give the lower boundary of the phase accuracy. Second, this boundary increases linearly by the external source of noise, in particular, the noise variance $\langle (\Delta N_T)^2 \rangle$.

Experimental results supporting the previous theoretical work are depicted in **Figure 24**. The classical and quantum images superimposed at different ratios (r) are shown in the first row. The second row shows the distilled images from the top row. Lastly, the third row displays transversal cuts of the distilled images. It is evident from these experimental results that images taken via QHUL become resilient to high intensities of noise. Also, the object phase variance increases proportionally to the noise. The article proved that this distillation technique works even for noise intensities 250 times higher than the signal of interest. For more experimental results, see ref. [28].

6.3. Phase-Quadrature Quantum Holography

Quantum holography with undetected light can also be implemented without changing the optical path, i.e., by taking only one image. Reference [27] presents a parallel quantum holography technique that implements a 4-step algorithm using a

2300353 (15 of 29)

**ADVANCED
SCIENCE NEWS**

www.advancedsciencenews.com

**ADVANCED
QUANTUM
TECHNOLOGIES**

www.advquantumtech.com

Figure 22. Results of QHUL by employing different algorithms. a) Images retrieved by QHUL with $M = 3$, 4, 6, and 12 steps. The detection time is also varied to $T_D = 100$, 200, 500, and 1000 ms. b) Phase accuracy of QHUL for two objects with phase steps of 0.62π and 0.82π. The black dashed lines are the expected experimental results. Each data point (•, ×) represents an average of 15 images retrieved with QHUL, and the error bars are their variances. Different colors represent the algorithm steps. From the experimental results, it can be observed that using a higher number of steps increases the phase accuracy of the retrieved images. Reproduced with permission.[26] Copyright 2022, American Association for the Advancement of Science.

spatial multiplexing approach. In this case, the signal beam containing the object information is interferometrically split into four independent beams, each carrying a different relative phase, see **Figure 25**. These four beams are simultaneously detected on the camera, producing the four images required for quantum holography, see Equations (34)–(37).

One benefit of this technique is that, by requiring only one image acquisition, it speeds up the holography process. This can be useful for highly dynamic samples where PSDH cannot be implemented. Lastly, a drawback of this scheme is that the algorithm (number of steps) is rigid and cannot be easily changed.

7. Additional Techniques in Quantum Sensing and Quantum Information Science

Besides quantum imaging, QUIL has inspired the development of many other techniques with undetected photons, such as spectroscopy,[21] sensing,[24] optical coherence tomography,[22] or

polarimetry.[100] In the following, we introduce some of these techniques, detailing their main features.

7.1. Spectroscopy

In 2016, D. A. Kalashnikov *et al.* introduced the first experimental implementation of infrared spectroscopy by detecting visible light.[21] Their setup consists of two identical sources of length L_z, collinearly aligned and longitudinally separated by a distance L_m; see **Figure 26** (left). The sources are embedded in a chamber filled with a gas of interest (CO_2). In type-0 processes, photon pairs are emitted with an emission angle given by the quasi-phase-matching condition contained in the sinc function, see Equation (1). After the signals leave the chamber, a spectrograph collects them and delivers their angular-wavelength dependency. The collected signal photon intensity is

$$\langle N_S(\lambda_S, \theta_S) \rangle \propto \tfrac{1}{2}\mathrm{sinc}^2\left(\tfrac{\delta}{2}\right)\{1 + |T_I^m|\cos(\delta + \delta^m)\} \tag{43}$$

where

$$\delta(\lambda_S, \theta_S) = (\mathbf{k}_P - \mathbf{k}_S - \mathbf{k}_I)L_z \tag{44}$$

$$\delta^m(\lambda_S, \theta_S) = (\mathbf{k}_P^m - \mathbf{k}_S^m - \mathbf{k}_I^m)L_z \tag{45}$$

$\mathbf{k}$ and $\mathbf{k}^m$ are the wavevectors in the SPDC nonlinear medium and the free-space propagation inside the chamber, respectively. These wavevectors have a dependency on the refractive indexes, i.e., $\mathbf{k} \to \mathbf{k}(n)$ ($\mathbf{k}^m \to \mathbf{k}^m(n^m)$). $|T_I^m| \propto \exp(-\alpha_I^m L_m)$, where α_I^m is the gas absorption coefficient with respect to the idler photon. This coefficient can be associated with the angular-wavelength visibility obtained by the signal photon interference, see Equation (43). Here absorption and dispersion of idler photon and pump beam are neglected.

In ref. [21], the following central wavelengths are chosen: $\lambda_P = 532$ nm, $\lambda_S = 608$ nm, and $\lambda_I = 4.28$ μm. These wavelengths were selected due to CO_2 absorption at 4.28 μm. Figure 26 (right) shows the experimental results. Figure 26a (right) shows the signal visibility after passing the chamber without gas (in vacuum). These values are employed as a reference for the initial visibility. Figure 26b (right) shows the signal visibility after passing the chamber with a concentration of 7.7 torr of CO_2. From the two cross-section visibilities in Figure 26a,b, it is evident that the CO_2 has absorbed idler photons, diminishing the signal visibility. In general, we have that the idler absorption is related to the signal visibility by

$$\alpha_I^m = -\frac{\ln(\mathcal{V}_S)}{L_m} \tag{46}$$

Spectroscopy with undetected light has been expanded into several directions, such as implemented in a SU(1,1) interferometer,[101] with seed lasers,[102–104] with enhanced pump beam,[105] with crystal superlattices,[106] and with probing photons at terahertz wavelengths.[25] One technique of particular physical interest is "Fourier transform spectroscopy," detailed next.
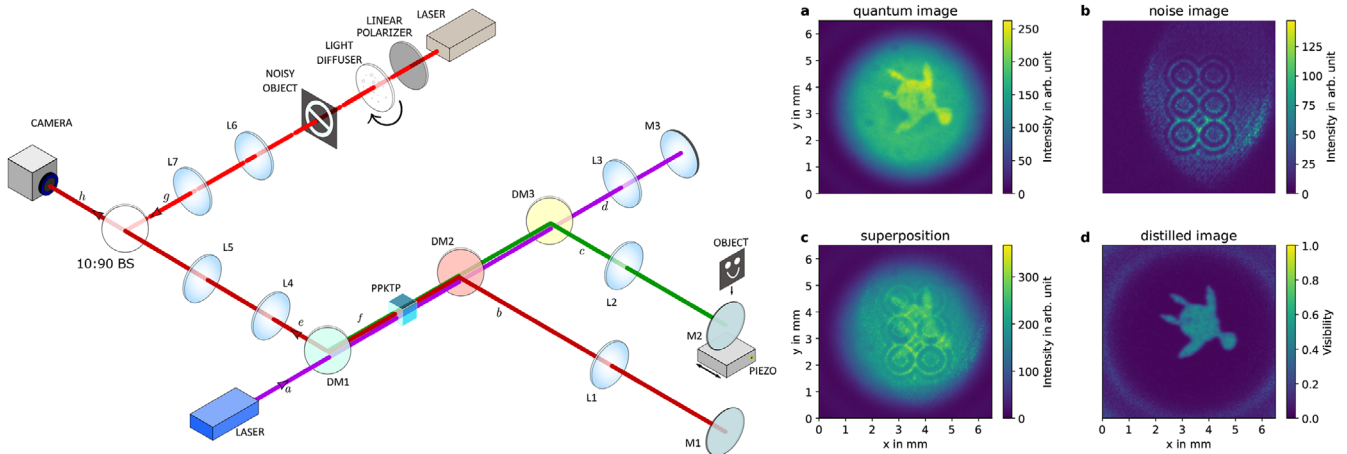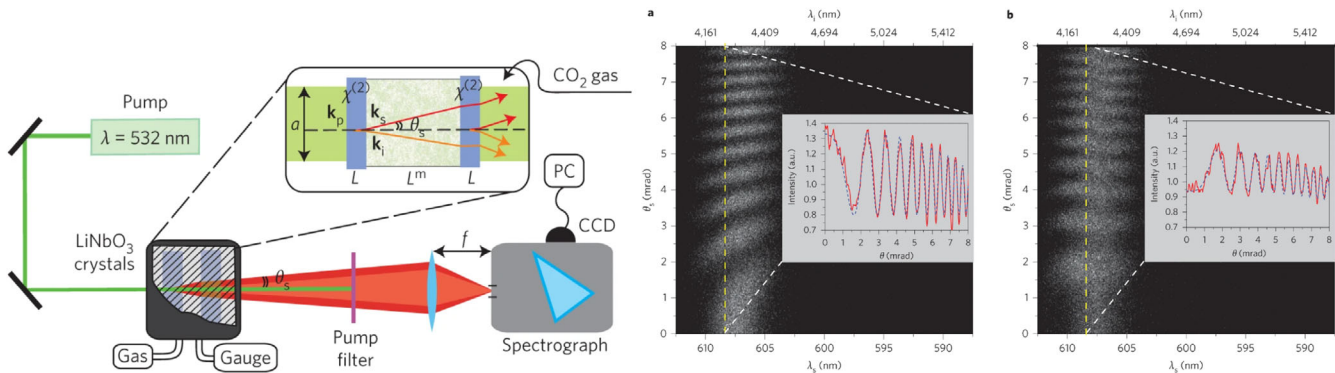
Figure 23. Setup and distillation principle. a) Quantum image. b) Classical image. c) Superposition of images (a) and (b). d) Distilled quantum image from (c). Reproduced with permission.[28] Copyright 2022, American Association for the Advancement of Science.
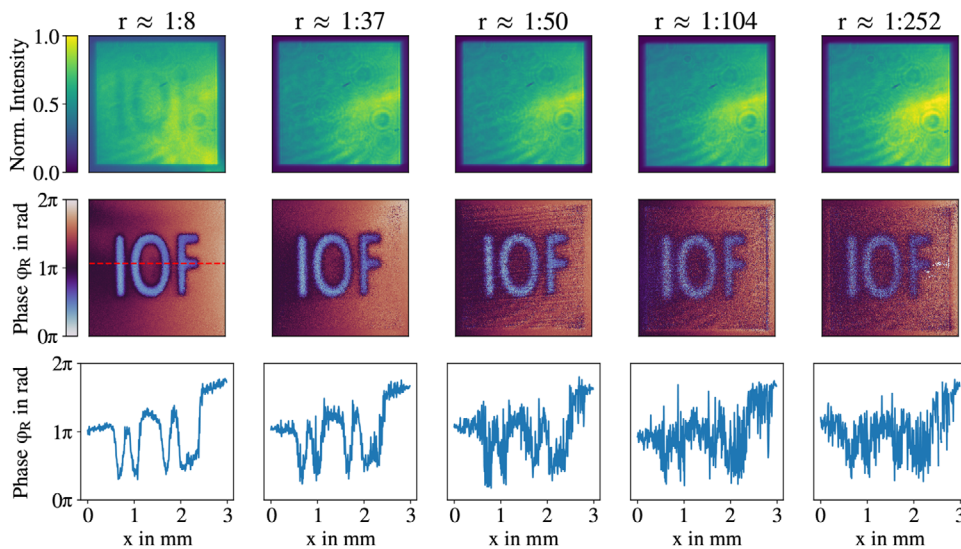
Figure 24. Experimental quantum imaging distillation with undetected light. The first row shows the superposition of quantum and classical images at different ratios (r) between their intensities. From left to right, the noise intensity increases. The second row shows the distillation results of the quantum images. The third row shows a transversal cut of the previous distilled images. Reproduced with permission.[28] Copyright 2022, American Association for the Advancement of Science.
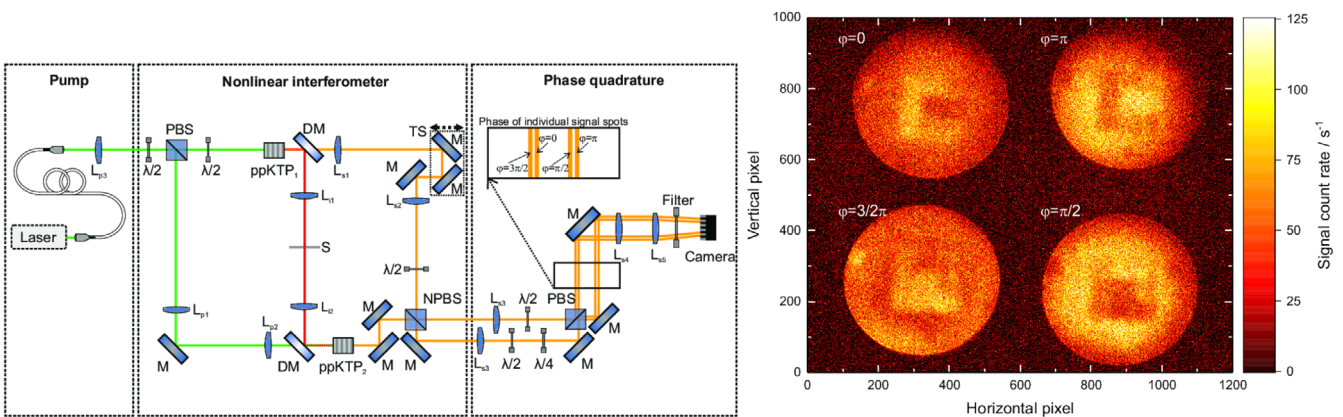
Figure 25. Phase-quadrature quantum holography with undetected light. Reproduced with permission.[27] Copyright 2022, Optica.

ADVANCED
SCIENCE NEWS
www.advancedsciencenews.com

ADVANCED
QUANTUM
TECHNOLOGIES
www.advquantumtech.com

Figure 26. Infrared spectroscopy with undetected light. Reproduced with permission.[21] Copyright 2016, Springer Nature Limited.

7.1.1. Fourier Transform Spectroscopy with Undetected Light

Fourier transform spectroscopy with undetected light (FTSUL) was introduced by C. Lindner *et al.*[107] The authors employed an SU(1,1) interferometer as depicted in **Figure** 27a, which is alike to a M-QIUL implementation. Idlers probe the object, while pump beam and signals are reflected and never interact with the object. In this case, the object of interest has only a spectral dependency, producing the absorption of some idlers. After the three beams (idler, signal, and pump) have returned to the nonlinear medium, a camera collects the signal, and the idler and pump are discarded. The arrival position of the signal photon on the camera depends on the emission angle in the SPDC process shown in Figure 27b. Consequently, a wide-field of signals is formed; see **Figure** 28a. A piezo located below the idler's end mirror (M_i) changes the interferometric phase in the nonlinear interferometer. If the indistinguishability conditions are fulfilled (see Section 2.3.3), signals on the camera show an interference pattern that varies with the piezo's position. Signal counts for these phases are shown in Figure 28b. As we can observe, the signal photon interference also varies at different periodicities depending on the camera pixel position that collects them. Signals at the center of the beam have smaller periods than signals far from it. By applying a Fourier transform on the data set, it can be obtained the wavelength information which is presented in Figure 28c. This technique allows a considerable increment in the range of probing wavelengths.
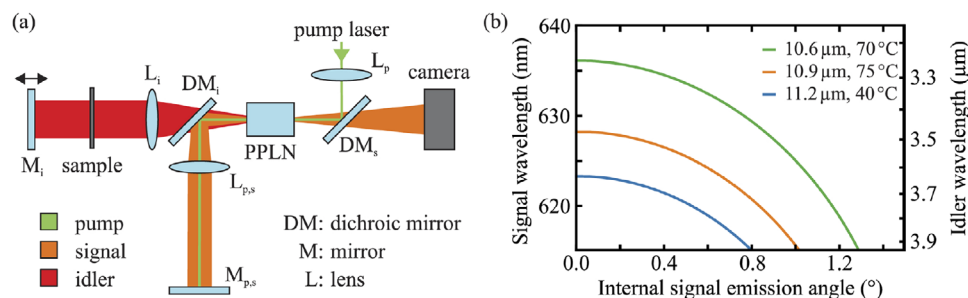
FTSUL has been implemented with a single-pixel detector[108,109] and with a NIR grating;[110] it also has been expanded into holography,[111] and realized with probing photons in the fingerprint region ($\approx$6–20 μm).[112]
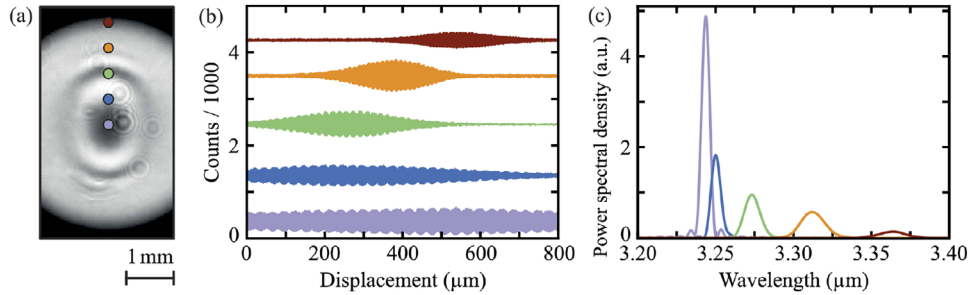
7.2. Optical Coherence Tomography

Optical coherence tomography (OCT), originally introduced in bio-imaging,[113] is a technique that allows the extraction of a tissue's 3D information. OCT employs beams with short coherent lengths, large bandwidth, and long wavelengths for optical sectioning. The effect of long wavelengths is reflected in their larger axial resolution and, therefore, deeper penetration in the tissue. All these three light characteristics can be achieved by using SPDC. The implementation of OCT in a nonlinear interferometer obtains the benefit of deeper penetration in tissues while detection is carried out in the visible spectrum. Optical coherence tomography with undetected light (OCTUL) was simultaneously introduced by two groups using different configurations.[22,23]

The first OCTUL implementation introduced by A. Valles *et al.* is depicted in **Figure** 29 and uses a ZWM interferometer. Similar to other techniques based on nonlinear interferometers, a photon pair is emitted in a quantum superposition of sources Q1 and Q2 ($PPLN_1$ and $PPLN_2$, respectively, in Figure 29 (left)). The SPDC process is type-0 and non-degenerate, emitting vertically polarized photon pairs. The PBS_1 reflects the idler beam emitted in Q1; its polarization is rotated to circular by a QWP and illuminates the sample. The polarization of the idler photons scattered by the object is rotated to horizontal, and the following HWP_I returns its polarization to vertical. In this way, the idler polarization modes are indistinguishable at Q2. The signal beam from

Figure 27. Fourier transform spectroscopy Reproduced with permission.[107] Copyright 2020, Optica.

**ADVANCED
SCIENCE NEWS**

www.advancedsciencenews.com

**ADVANCED
QUANTUM
TECHNOLOGIES**

www.advquantumtech.com

Figure 28. Fourier transform spectroscopy results. Reproduced with permission.[107] Copyright 2020, Optica.

Q1 passes a stage able to change its optical path, and an HWP rotates its polarization to horizontal. Both signal beams carrying orthogonal polarizations are recombined in the same path with the help of PBS$_2$. Then these signals traverse a linear polarizer with its angle oriented at diagonal polarization. Here, the signal state goes from a pure state to a totally mixed state, depending on the mutual coherence of the signal beams. The mutual coherence is varied by changing the optical path distance, as shown in Figure 29 (right). The purity of the signal state is proportional to its amplitude interference. In this way, the axial information of a sample is directly linked to the signal photon induced coherence.

The second OCT experiment introduced by Anna V. Paterova et al. is depicted in **Figure 30** (top) and uses an SU(1,1) interferometer.[23] This article presents a thorough analysis of the axial resolution both theoretically and experimentally. Similarly to previous techniques, the authors derived the signal photon intensity as

$$\langle N_S \rangle \propto [1 + f(R, T)|\mu(\Delta t)| \cos(\delta_{in})] \quad (47)$$

where $f(R, T)$ is a reflection/transmission function through the sample, $|\mu(\Delta t)|$ is the width of the correlation function, Δt is the time difference of signal and idler photons inside the interferometer, and $\delta_{in} = \delta_S + \delta_I - \delta_P$. $\mu(\Delta t)$ is the Fourier transform of the SPDC spectrum and has the form[23,45]

$$\mu(\Delta t) = 2\pi \int d\Omega \, S(\Omega) \, e^{(-i\Omega\Delta t)} \quad (48)$$

$S(\Omega)$ is the SPDC spectral intensity, and Ω is the frequency detuning. Since the axial resolution is linked to $|\mu(\Delta t)|$, and the bandwidth of the SPDC photons governs the latter, the axial res-

olution takes the shape of a triangular function, as shown in Figure 30 (bottom); see also ref. [114]. This effect was proven for different pairs of SPDC wavelengths and coherence lengths. OCTUL has been further expanded in the high-gain regime[115] and has also found some advantages when the bi-photon state becomes separable.[64] More details of OCT in high gain are discussed in Section 8.1.

7.2.1. Frequency Domain Optical Coherence Tomography

The two previous OCTUL techniques (refs. [22] and [23]) work in the time domain. In 2020, A. Vanselow et al.[116] introduced an OCTUL technique in the frequency domain using mid-infrared undetected idler photons. A few differences exist between the time and frequency domain OCT's configurations, mainly in the acquisition and post-processing stages. For example, Vanselow employed a spectrometer to record the signal intensity and later performed a Fourier transform to obtain the spectral information of the sample.

The frequency domain OCT setup is sketched in **Figure 31** and uses an SU(1,1) interferometer. Figure 31b (top) shows the raw intensity in the first inset and the corresponding Fourier transform post-processed signal amplitude in the second inset. This OCT technique is tested on 2D and 3D alumina ceramic structures and paintings of several layers. This work also performs a study of both axial and transverse resolutions. The authors showed an axial resolution of 11 μm (FWHM) and a transverse resolution of 19 μm (FWHM of a point-spread function) for the set of wavelengths (signal: 785-823 nm, idler: 3.33–4.15 μm). Experimental results for axial and transverse resolutions are shown in Figure 31b (bottom),c (i,ii, bottom), respectively.
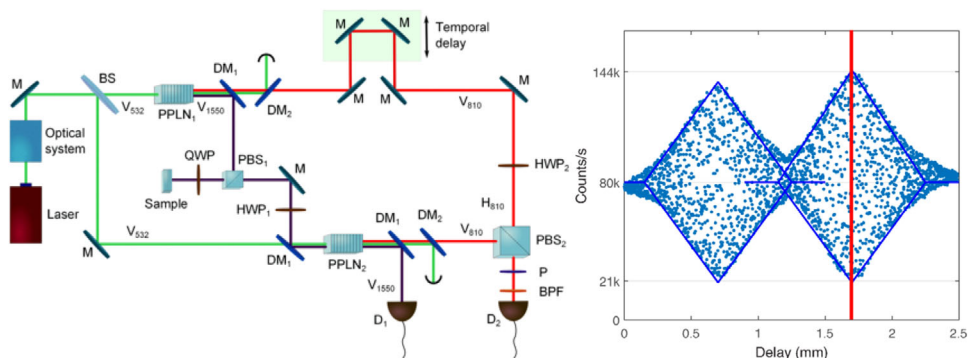
Figure 29. Optical coherence tomography in a ZWM interferometer Reproduced with permission.[22] Copyright 2018, American Physical Society.
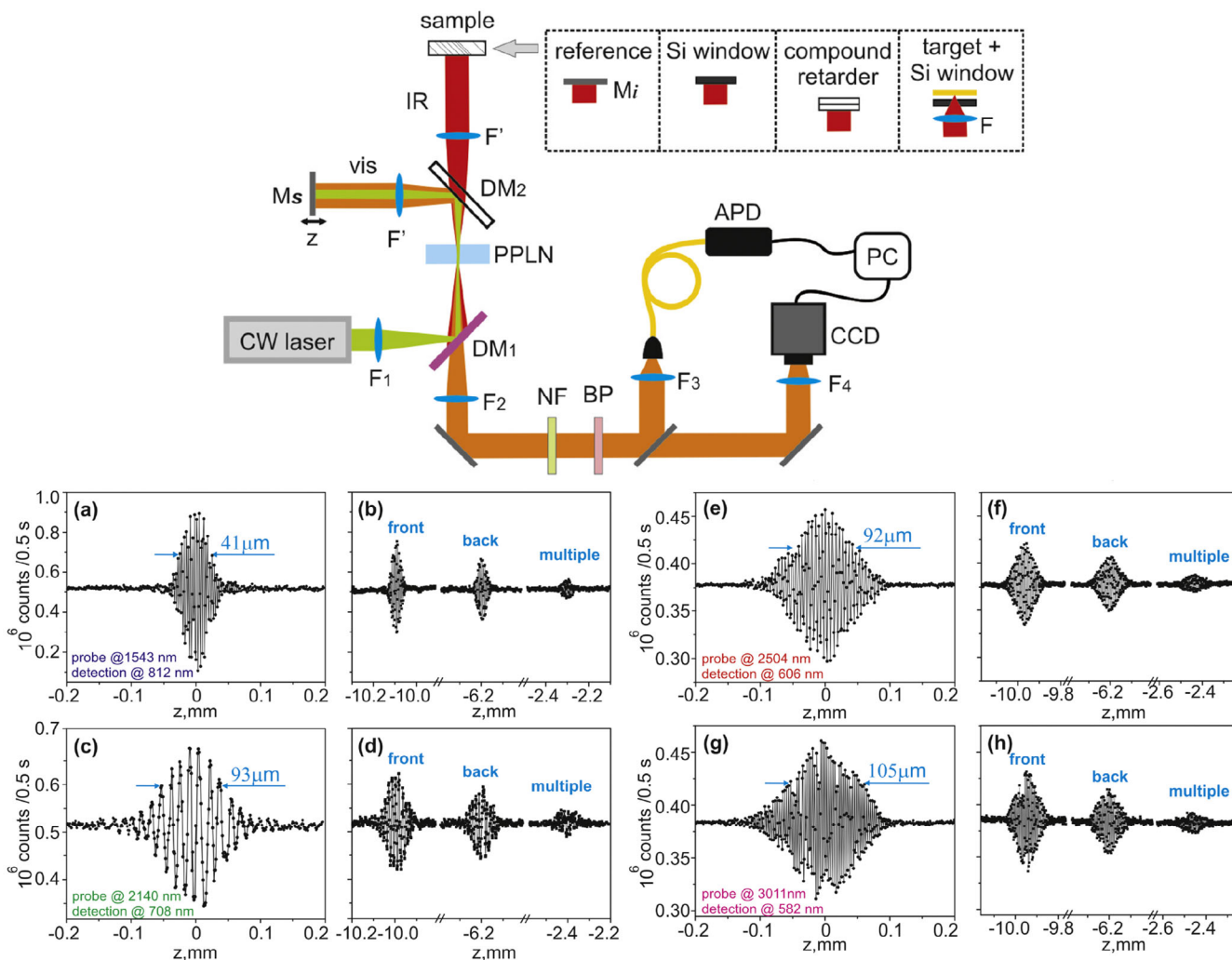
Figure 30. Optical coherence tomography in an SU(1,1) interferometer Reproduced with permission.[23] Copyright 2018, IOP Publishing Ltd.

Lastly, the reader could find useful a comprehensive study comparing three different implementations of frequency domain OCT in the low- and high-regime: Classical OCT, Zou–Wang–Mandel interferometer, and SU(1,1) interferometer based OCTs.[117]

7.3. Sensing

Since every technique based on the induced coherence effect uses a nonlinear interferometer, it is well-known that the phase information of a sample can also be obtained. However, in an outstanding source engineering work, M. Kutas *et al.*[24] proved that sensing can be performed with terahertz photons while visible photons are detected. Note here that terahertz photons are not only generated by quantum fluctuations and, therefore, the mathematical derivation slightly differs from usual SPDC processes; for more details, see ref. [118]. This sensing setup is depicted in **Figure 32** (left).

The authors employed an SU(1,1) interferometer, pumping a PPLN crystal with a 659.58 nm pump beam and generating

photon pairs in the visible and terahertz spectra. In Figure 32 (left), it can be observed the angular spectra of both tails of the Stoke and Anti-stoke regions corresponding to the down- and up-conversion processes, respectively. Different polytetrafluoroethylene (PTFE) plates were chosen to test this technique. By placing these objects in the idler path, the signal photon interference is destroyed because of the additional optical path the terahertz photon has to traverse. Therefore, by compensating this optical path with a mechanical translation stage, it was possible to determine the thickness of the samples. Figure 32 (right) shows experimental results for samples with different thicknesses measured with traditional and quantum sensing techniques. The results show an excellent agreement between these two techniques and pave the way for quantum sensing in industrial applications.

7.4. Works with Polarization

Even though polarization is a well-known degree of freedom, there are few works studying it in nonlinear interferometers. Here, we present a brief introduction of them.
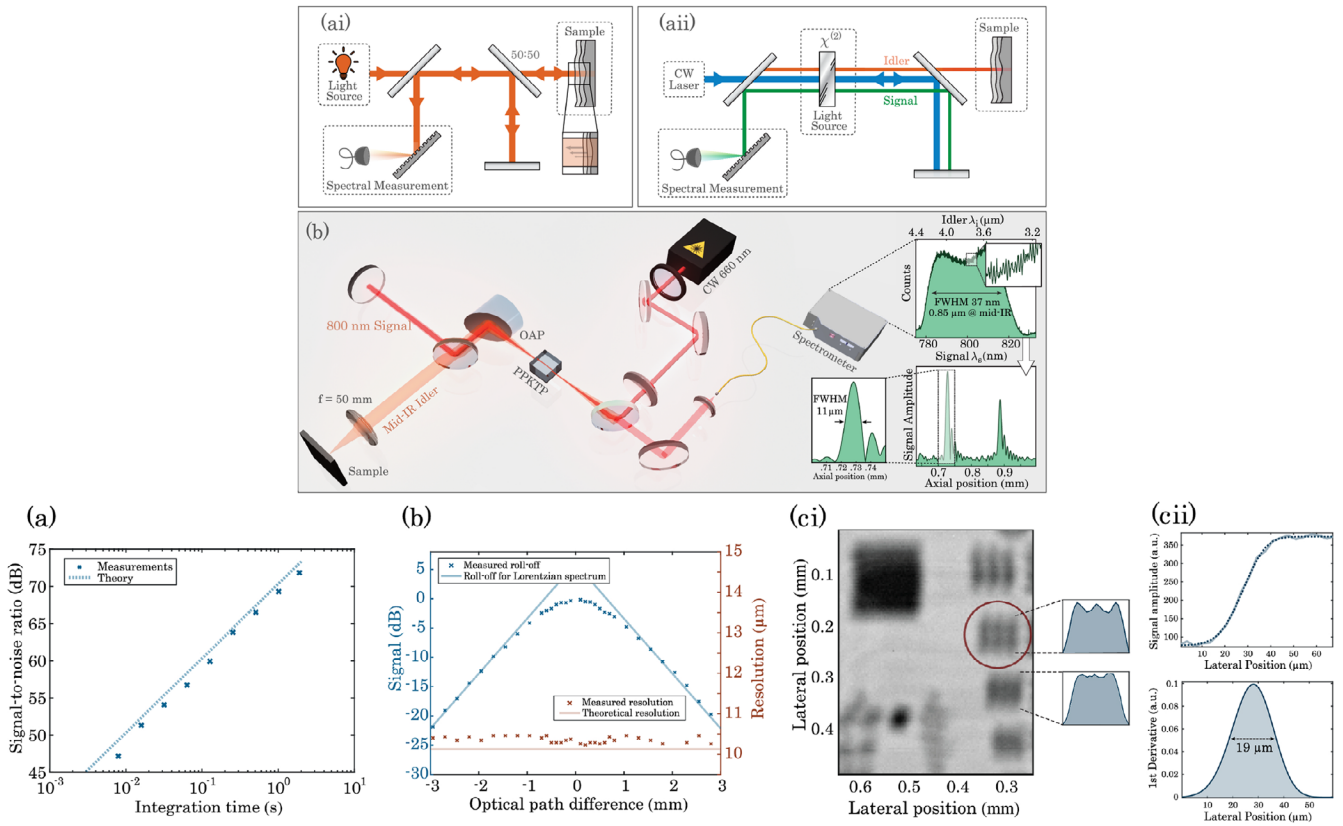
**ADVANCED
SCIENCE NEWS**

www.advancedsciencenews.com

**ADVANCED
QUANTUM
TECHNOLOGIES**

www.advquantumtech.com

Figure 31. Frequency domain optical coherence tomography. Reproduced with permission.[116] Copyright 2020, Optica.

7.4.1. Characterization of Plate Retarders

The absence of coherence in an induced coherence scheme also can be utilized in different applications. A. V. Paterova et al.,[100] using an SU(1,1) interferometer, introduced different techniques to obtain the retardation of a sample, in this case, plate retarders.

In the following, we briefly explain her experiment. For simplicity, let us consider an initial polarization state emitted in the crystal as $|H_I\rangle|H_S\rangle$, where H denotes horizontal polarization. The first technique is based on relative phases between different interferograms. The plate retarder of interest is placed in the idler path inside the nonlinear interferometer; see **Figure 33** (left). Thus, the idler photon passes twice through the sample in the forward and backward directions. In this way, the initial

state $|H_I\rangle$ obtains a transformation depending on the plate retarder and its angle θ. The interferometric phase is changed by moving one of the end mirrors (M_p, M_i, or M_s), and an interference pattern is obtained for each θ. From here, the relative phase between different polarization dependent interference patterns and the visibility can be extracted. Figure 33 (right) shows the experimental results for a quarter-wave plate (QWP) and a half-wave plate (HWP). The first plot shows the interference patterns (QWP – top; HWP – bottom) at the angles $\theta = 0°$, 45°, and 90°. The second plot shows the visibilities (QWP – blue; HWP – red). Since the double pass through an HWP produces a unitary transformation of the polarization at any angle, the initial and final states are the same, e.g., $|H_I\rangle_{\text{initial}} = |H_I\rangle_{\text{final}}$; this is evident from both experimental results. On the other hand, for different
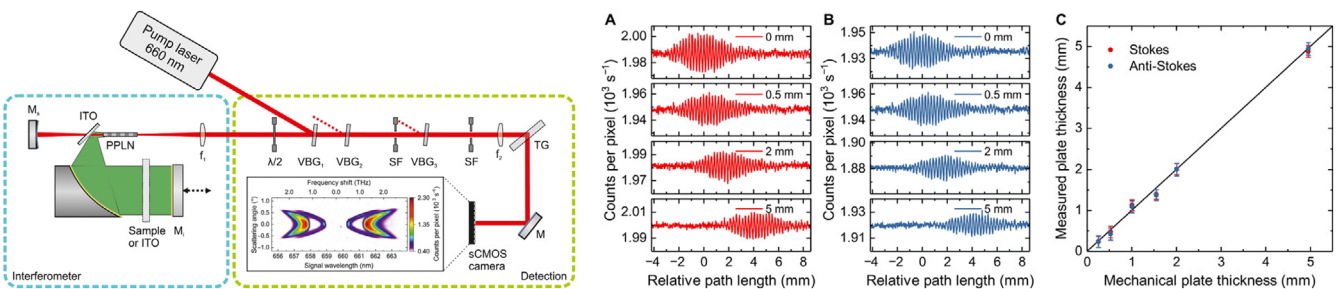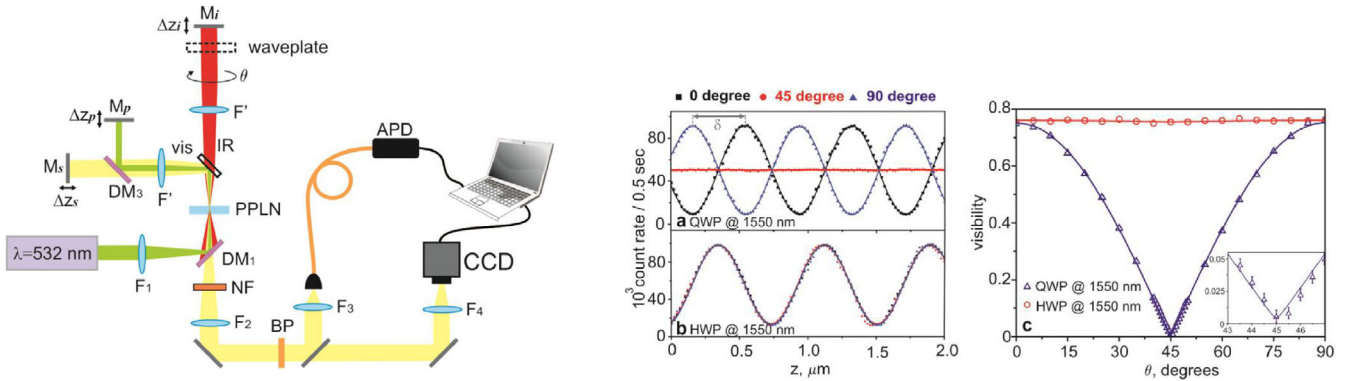

Figure 32. Terahertz sensing with undetected light. Reproduced with permission.[24] Copyright 2020, American Association for the Advancement of Science.

**ADVANCED
SCIENCE NEWS**

www.advancedsciencenews.com

**ADVANCED
QUANTUM
TECHNOLOGIES**

www.advquantumtech.com

Figure 33. Characterization of plate retarders via induced coherence. Reproduced with permission.[100] Copyright 2019, Optica.

angles θ of a QWP, notorious changes are obtained. The ellipticity added by this plate in the forward pass is later converted into vertical polarization in the backward pass, reaching a total conversion at $\theta = 45°$. This is also clearly shown in the experimental results, where for $\theta = 45°$, maximum distinguishability and, therefore, null visibility is obtained. The authors in the paper emphasized that this technique met high precision standards, comparing their experimental results with the providers' information. The second technique is also similar, and more details can be found in ref. [100].

7.4.2. Quantum State Tomography

Induced coherence has been mostly employed to obtain information about an object through the interaction of an idler photon with it, and in this review, we have explored many approaches. Nevertheless, it is important to understand that this is not the only application of this quantum effect.

A. Zeilinger's group, in a series of experiments, has shown the possibility of obtaining the "state information" of a single- or a two-photon quantum system. As in the previous cases, the idler photon remains undetected. In this way, two-photon momentum quantification,[35,62] two-photon entanglement certification,[119,120] and the quantum state tomography of a single photon[121] have been introduced. In this section, we review the latter related to the polarization degree of freedom.[121] For more details about these techniques, see ref. [44].

Without loss of generality, we can write the idler state of interest as

$$\hat{\rho}_I = \begin{pmatrix} P_H & \mathscr{I}\sqrt{P_H P_V}e^{-i\xi} \\ \mathscr{I}\sqrt{P_H P_V}e^{i\xi} & P_V \end{pmatrix} \qquad (49)$$

where P_H (P_V) is the probability of detecting an idler photon with horizontal (vertical) polarization, with $P_H + P_V = 1$; $\xi \in [0, 2\pi)$ is the relative phase between horizontal and vertical polarizations, and $\mathscr{I} \in [0, 1]$ is the decoherence term related to "dephasing."[122]

The idea of this experiment was to transfer the state information of the idler photon to its partner signal. In order to do so, one can build a reference state for the degree of freedom of interest. For polarization, it suffices to augment the source Q2 by adding a nonlinear crystal, see **Figure 34**. In this way, source Q2 produces

the following state

$$|\psi_2\rangle = \frac{1}{\sqrt{2}}(|H_{I2}\rangle|H_{S2}\rangle + |V_{I2}\rangle|V_{S2}\rangle) \qquad (50)$$

Signal paths are recombined, and each polarization component is measured independently at D1 and D2. The signal photon intensities are

$$\langle N_H \rangle = \frac{1}{4}\left(1 + |T_H|\sqrt{P_H}\cos(\phi)\right) \qquad (51)$$

$$\langle N_V \rangle = \frac{1}{4}\left(1 + \mathscr{I}|T_V|\sqrt{P_V}\cos(\phi + \xi)\right) \qquad (52)$$

$\langle N_H \rangle$ and $\langle N_V \rangle$ are the horizontal and vertical polarization-dependent interference patterns of the signal photon, respectively. Note that all information needed to reconstruct the idler state in Equation (49) is contained in Equations (51) and (52). Therefore, the polarization state of the idler is transferred to the signal photon as polarization-dependent coherence. The tomography technique was tested with different states prepared by HWP and QWP retarders, see Figure 34. Linearly polarized states obtained a mean fidelity of 0.97. For elliptically polarized states, the mean fidelity was about 0.92. These experimentally obtained fidelities validate this technique.

Since this tomography technique is based on quantum interference, it also should be suitable to, first, other phonics' degrees of freedom (e.g., orbital angular momentum and vector beams) and, second, other quantum entities such as atoms, ions, or molecules. More details in ref. [121].

Also introduced by the group of A. Zeilinger, the interplay between the polarization of signal and idler photons and coherence was studied in ref. [123].

8. Open Issues

8.1. High Gain Regime—Induced Emission

If both crystals of a nonlinear interferometer are pumped in the low-gain regime, emission in the second crystal is not induced in lowest order,[16] that is, the spontaneous regime, so that it makes no difference whether both signal and idler modes are used as

**ADVANCED
SCIENCE NEWS**

www.advancedsciencenews.com

**ADVANCED
QUANTUM
TECHNOLOGIES**

www.advquantumtech.com
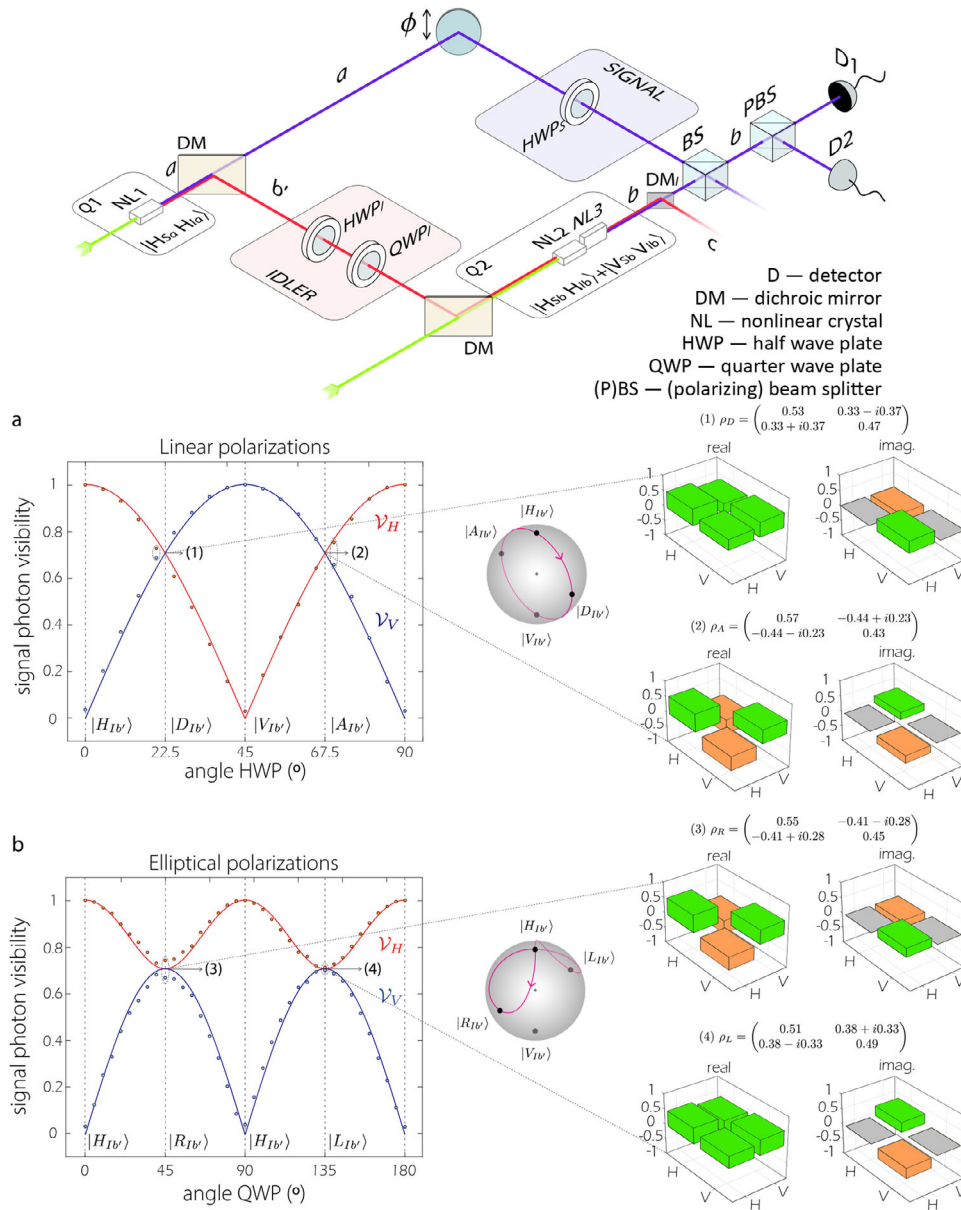
Figure 34. Quantum state tomography of undetected photons: setup and experimental results. Reproduced with permission.[121] Copyright 2024, The American Physical Society.
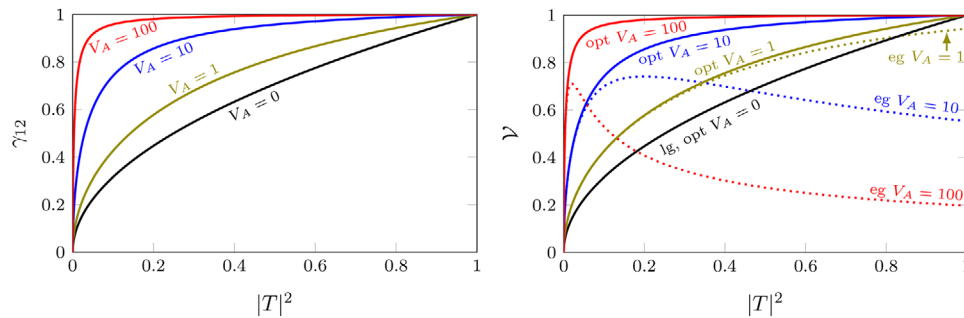
an input, or just one of them. Hence, there is no fundamental difference[117] between the induced-coherence setup like the original ZWM interferometer[13] with its imaging applications[12] and an SU(1,1) interferometer[43] where both signal and idler modes are used as an input of the second crystal. However, in the high-gain regime, both type of setups differ fundamentally,[117] as highlighted in the present section.

Already after the first experiments studying induced coherence, the role of induced emission for high gain was directly pointed out.[51] In principle, first-order coherence persists in both regimes. However, whether the effect is a classical or a quantum effect and whether emission is stimulated or not, was at the center of debate.[16,124] Driving the nonlinear processes with a strong (coherent) laser of course makes it possible to generate more than

just one photon pair in the whole setup. While this fact might open discussions whether emission is classical or not, from an operational point of view this question is of minor relevance. One should rather study if there are benefits for imaging in the high-gain regime. Some of them are obvious: It constitutes a way to increase the photon flux and by that the signal, as well as the signal-to-noise ratio.

Since both setups differ in this regime, we have to discuss their implications separately. For the ZWM interferometer, coherence persists for high gain.[51] **Figure 35** shows on the left the first-order coherence function for different gain as a function of the transmittance of the object. However, because the second crystal is seeded by one mode, the intensity of its output modes is larger than that of the first one. When interfering now one

ADVANCED
SCIENCE NEWS

www.advancedsciencenews.com

ADVANCED
QUANTUM
TECHNOLOGIES

www.advquantumtech.com

Figure 35. Coherence and visibility of an high-gain ZWM interferometer. The first-order coherence function γ_{12} between both arms before the last beam splitter increases for increasing parametric gain ξ in the first crystal for all values of the transmission $|T|$ (left panel). The gain is encoded in the parameter $V_A = \sinh^2 \xi$ and the limit $V_A \to 0$ describes the spontaneous regime, also shown in **Figure 4**. However, this increase does not necessarily lead to an increased visibility $\mathcal{V}$ after interference, because both beams may possess different intensities at the beam splitter (right panel). The dotted lines show the visibility when the gain of both crystals is the same (e.g., equal gain). In the high-gain regime, the visibility drops for large transmission. This deleterious effect can be mitigated by optimizing the gain at the second crystal, so that the visibility reproduces the first-order coherence (opt, solid lines). Reproduced with permission.[126] Copyright 2017, IOP Publishing.

output mode of the second crystal with the output mode of the first crystal on a beam splitter, both will have different intensities and therefore the visibility drops,[125] even though the light is still coherent. To nevertheless obtain optimal visibility, one can simply adjust the gain in the second crystal,[126] see Figure 35, so that the overall visibility exactly corresponds to the first-order coherence function. A similar strategy can be applied to amplitude imaging, where also the seed of the second crystal is reduced depending on the transmittance of the object. With such an approach, the signal-to-noise ratio can be increased significantly. In principle, one can also think about an intermediate setup, where one crystal is operated in the high-gain regime, while the other emits spontaneously. Obviously, such an operation leads to a decreasing visibility,[126] but nevertheless low-coherence interferometry has been performed and characterized.[127]
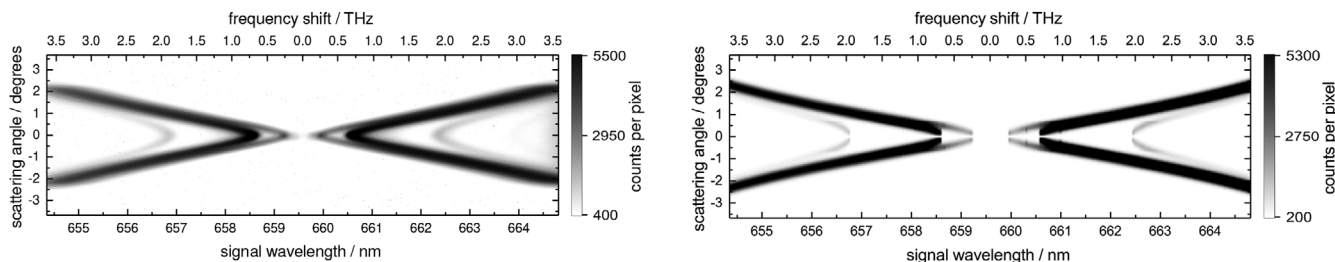
In contrast, the SU(1,1) interferometer allows for a symmetric seed of the second crystal, at least if the inserted object has perfect transmittance. In this case, both modes are further amplified or deamplified. This setup has drawn major attention, because it has been shown in a one-mode theory without loss to achieve phase supersensitivity close to destructive interference,[43] that is, a phase sensitivity below shot noise approaching the Heisenberg limit. This superb sensitivity is achieved by a two-mode squeezed vacuum generated in the first crystal, followed by perfect anti-squeezing in the second one back to vacuum, which can be interpreted as a time-reversed operation.[128,129] Because of a possible sub-shot-noise sensitivity of phases, SU(1,1) interferometers pose a promising alternative for phase imaging based on quantum-metrological approaches.[130]

Since the generated squeezed vacuum state is, like other quantum states, susceptible to noise, the phase supersensitivity quickly degrades for internal or detection loss.[131] By unbalancing the gain between both crystals, such deleterious effects have been partially compensated,[132] even though it is difficult to still associate a Heisenberg-type scaling to the phase sensitivity.[133] For a complete assessment of the capabilities of such a quantum-metrological approach, one also has to see the pump as the fundamental resource and part of the overall light budget.[134,135] Despite all these subtleties, the benefits of SU(1,1) interferometers have been observed experimentally.[115,132,136]

However, while most theoretical studies focus on a single-mode description of high-gain parametric down-conversion, it is inherently multimode in nature,[137–139] which is in fact an advantage for imaging. For the generation of parametric down-conversion in the high-gain regime,[140–142] the generation of such a bright squeezed vacuum[143] with mesoscopic photon numbers can also be enabled by an SU(1,1) interferometer[144] and its spatial and spectral properties can be tailored to amplify specific parts of the (spatiotemporal) spectrum in the second crystal.[145,146] Because time-ordering issues arise,[147] the theoretical description of high-gain parametric down-conversion and SU(1,1) interferometers is subtle and often approached by a Bloch-Messiah reduction or Schmidt-mode decomposition.[148–151] The main reason is that the eigenmodes of squeezing change upon propagation through the crystals. Of course, the multimode nature of the generated light can have a deleterious effect on the phase sensitivity,[152] so that it is important in high gain to perfectly match the modes between both crystals.[153] This can be implemented by imaging the output of the first crystal into a second one, giving rise to the experimental demonstration of wide-field SU(1,1) interferometry.[136]

The technique of optical coherence tomography (OCT), already introduced in Section 7.2, has also been extended to the high-gain regime. It has been theoretically analyzed for the ZWM setup as well as an SU(1,1) interferometer and compared to the standard procedure, that of course does not work with undetected light.[117] In fact, due to amplification in the crystal in case of the SU(1,1) setup, the detected signal can be larger than the light that interacted with the object, but in this case the device is not operated at the point of optimal phase sensitivity. The experimental realization[115] of OCT with this symmetric scheme studied the visibility of the interference pattern as a function of transmission of the object and gain. A decrease in visibility was observed, similar to the case of the ZWM interferometer as explained above. In this type of amplitude imaging, a higher signal-to-noise ratio was achieved, but phase supersensitivity was not demonstrated. Moreover, the setup also allowed for OCT in the frequency domain, which has already been transferred to broadband spectroscopy.[154]

**ADVANCED
SCIENCE NEWS**

www.advancedsciencenews.com

**ADVANCED
QUANTUM
TECHNOLOGIES**

www.advquantumtech.com

Figure 36. SPDC emission spectra experimentally obtained (left) is in excellent agreement with the numerical modelling (right). Reproduced with permission.[118] Copyright 2019, Optica.

Another approach to boost the signal and sensitivity of imaging with undetected light by seeding the input of the first crystal.[155] Since the seed is inducing emission through a coherent classical state, this technique is sometimes also referred to as "classical imaging with undetected light" and imaging experiments have been performed,[60,61] also in a ZWM-type of setup.[156] Similar to the unseeded case, gain unbalancing can be used for loss compensation and phase uncertainty below some Heisenberg-type scaling for the SU(1,1) geometry has been demonstrated.[157,158]

In this section, we have focused on conventional imaging techniques with undetected light based on intensity detection. However, quantum dense metrology with seeded SU(1,1) interferometers for simultaneous phase and amplitude measurements are possible, but require homodyne detection.[159]

8.2. Perspectives of QIUL

As one can see from the previous sections, QIUL is a practicable tool for various applications. Before discussing the potential use-cases in the future, one can have a look from a fundamental point of view on the most likely and most important next developments.

When designing optical systems, one can use various software solutions to optimize performance and footprint. It would be great to have a "quantum upgrade" of such optics design software such that nonlinear processes like SPDC are included. This way, a system design for practical purposes would be more convenient. For example, one could design a complete infrared microscope with visible light detection, which would help to bring this beautiful piece of quantum technology out of the lab into the market.

The linchpin of nonlinear interferometers is the SPDC source that requires a quantum optical treatment of the system. Here a lot of effort was put into making useful predictions such as the almost perfect description of the SPDC spectrum for signal and idler in the visible and THz, respectively as shown in **Figure 36**.[118] Further work in the same research group culminated in a "General Simulation Method for Quantum-Sensing Systems".[160] The numerical model allows us to account for experimental imperfections of nonlinear interferometers, like incorrect lens positions that influence interference visibility.[18] This allows us to estimate alignment tolerances for future industry-ready QIUL systems. Additional work demonstrated that interference visibility, coherence length, equal-inclination interference, and equal-thickness interference can be numerically calculated with simplified theoretical models and still yield sufficient agreement with experimental data.[161]

In contrast to that, refining the physical models dropping certain approximations may unveil important aspects, as one can see from the discussions in Sections 5.1.4 and 5.2. Therefore, it would be of interest to apply a full description of the SPDC process in a nonlinear interferometer. This particularly includes neglecting common approximations like assuming a plane wave for pump or even coherence of the pump beam.

On the application side, QIUL has the strong potential to develop new tools for imaging in extreme spectral ranges where detection is challenging. A prominent spectral domain is the mid-infrared, where detectors suffer from low efficiency compared to silicon-based counterparts for the visible range. In addition, due to thermal photons, the signal-to-noise ratio is poor and often requires cryogenic cooling, which is very cost-intensive. Hence, QIUL is a suitable alternative. This way, it has the potential to allow new tools for biomedical imaging. Since the idler beam is in the mid-infrared, it covers the molecular spectral fingerprint region and thus, allows for label-free chemical-selective imaging of bio-molecules like lipids or proteins with visible light detection. Of course, this requires a combination of imaging and spectroscopy capabilities to result in hyperspectral mid-infrared imaging with visible light. First attempts in this direction have been successfully carried out in the near-infrared region up to $\approx 3.5\,\mu m$.[19,20] An extension toward up to $\approx 10\,\mu m$ or further can be expected soon. The main obstacle is the material for the nonlinear crystal. While PPKTP and PPLN have their transparency window up to $\approx 3.5\,\mu m$, silver/lithium gallium sulfide (LGS/AGS) crystals are transparent up to $\approx 12\,\mu m$.[112]

When it comes to imaging applications, QIUL can be combined with sophisticated classical imaging approaches as it was demonstrated for holography (see Section 6). More adaptions of beneficial classical imaging techniques into QIUL will surely follow.

One of the strongest aspects of nonlinear interferometers for practical usage is that they can be manufactured with very small footprint by employing only standard components (laser, optics, and detector). This makes them attractive for novel use-cases like sensing on drones or for mobile (quantum) imaging devices.

Acknowledgements

**ADVANCED
SCIENCE NEWS**

www.advancedsciencenews.com

**ADVANCED
QUANTUM
TECHNOLOGIES**

www.advquantumtech.com

Conflict of Interest

The authors declare no conflict of interest.

Keywords

induced coherence, nonlinear interferometer, quantum imaging, quantum interference

[1] E. Abbe, *Arch. Mikrosk. Anat* **1873**, *9*, 413.
[2] S. Jin, W. Hui, Y. Wang, K. Huang, Q. Shi, C. Ying, D. Liu, Q. Ye, W. Zhou, J. Tian, *Sci. Rep.* **2017**, *7*, 45209.
[3] E. Betzig, G. H. Patterson, R. Sougrat, O. W. Lindwasser, S. Olenych, J. S. Bonifacino, M. W. Davidson, J. Lippincott-Schwartz, H. F. Hess, *Science* **2006**, *313*, 1642.
[4] M. Gilaberte Basset, F. Setzpfandt, F. Steinlechner, E. Beckert, T. Pertsch, M. Gräfe, *Laser Photonics Rev.* **2019**, *13*, 1900097.
[5] M. Kutas, B. E. Haase, F. Riexinger, J. Hennig, P. Bickert, T. Pfeiffer, M. Bortz, D. Molter, G. von Freyman, *Adv. Quantum Technol.* **2022**, *5*, 2100164.
[6] Y. Israel, S. Rosen, Y. Silberberg, *Phys. Rev. Lett.* **2014**, *112*, 103604.
[7] T. Ono, R. Okamoto, S. Takeuchi, *Nat. Commun.* **2013**, *4*, 2426.
[8] G. Brida, M. Genovese, I. R. Berchera, *Nat. Photon.* **2010**, *4*, 227.
[9] J. Zander, C. Rembe, R. Schnabel, *Quantum Sci. Technol.* **2022**, *8*, 01LT01.
[10] T. B. Gäbler, P. Hendra, N. Jain, M. Gräfe, *Quantum Sci. Technol. arXiv* **2023**, arXiv:2303.16584.
[11] D. Tabakaev, A. Djorović, L. La Volpe, G. Gaulier, S. Ghosh, L. Bonacina, J.-P. Wolf, H. Zbinden, R. T. Thew, *Phys. Rev. Lett.* **2022**, *129*, 183601.
[12] G. B. Lemos, V. Borish, G. D. Cole, S. Ramelow, R. Lapkiewicz, A. Zeilinger, *Nature* **2014**, *512*, 409.
[13] X. Y. Zou, L. J. Wang, L. Mandel, *Phys. Rev. Lett.* **1991**, *67*, 318.
[14] L. J. Wang, X. Y. Zou, L. Mandel, *Phys. Rev. A* **1991**, *44*, 4614.
[15] T. J. Herzog, J. G. Rarity, H. Weinfurter, A. Zeilinger, *Phys. Rev. Lett.* **1994**, *72*, 629.
[16] M. Lahiri, A. Hochrainer, R. Lapkiewicz, G. B. Lemos, A. Zeilinger, *Phys. Rev. A* **2019**, *100*, 053839.
[17] K. Qian, K. Wang, L. Chen, Z. Hou, M. Krenn, S. Zhu, X.-S. Ma, *Nat. Commun.* **2023**, *14*, 1480.
[18] M. Gilaberte Basset, A. Hochrainer, S. Töpfer, F. Riexinger, P. Bickert, J. R. León-Torres, F. Steinlechner, M. Gräfe, *Laser Photonics Rev.* **2021**, *15*, 2000327.
[19] I. Kviatkovsky, H. M. Chrzanowski, E. G. Avery, H. Bartolomaeus, S. Ramelow, *Sci. Adv.* **2020**, *6*, eabd0264.
[20] A. V. Paterova, S. M. Maniam, H. Yang, G. Grenci, L. A. Krivitsky, *Sci. Adv.* **2020**, *6*, eabd0460.
[21] D. A. Kalashnikov, A. V. Paterova, S. P. Kulik, L. A. Krivitsky, *Nat. Photon.* **2016**, *10*, 98.
[22] A. Vallés, G. Jiménez, L. J. Salazar-Serrano, J. P. Torres, *Phys. Rev. A* **2018**, *97*, 023824.
[23] A. V. Paterova, H. Yang, C. An, D. A. Kalashnikov, L. A. Krivitsky, *Quantum Sci. Technol.* **2018**, *3*, 025008.
[24] M. Kutas, B. Haase, P. Bickert, F. Riexinger, D. Molter, G. von Freyman, *Sci. Adv.* **2020**, *6*, eaaz8065.
[25] M. Kutas, B. Haase, J. Klier, D. Molter, G. von Freyman, *Optica* **2021**, *8*, 438.
[26] S. Töpfer, M. Gilaberte Basset, J. Fuenzalida, F. Steinlechner, J. P. Torres, M. Gräfe, *Sci. Adv.* **2022**, *8*, eabl4301.
[27] B. E. Haase, J. Hennig, M. Kutas, E. Waller, J. Hering, G. von Freyman, D. Molter, *Opt. Express* **2023**, *31*, 143.
[28] J. Fuenzalida, M. Gilaberte Basset, S. Töpfer, J. P. Torres, M. Gräfe, *Sci. Adv.* **2023**, *9*, eadg9573.
[29] D. N. Klyshko, *Sov. Phys. JETP* **1969**, *28*, 522.
[30] D. C. Burnham, D. L. Weinberg, *Phys. Rev. Lett.* **1970**, *25*, 84.
[31] S. P. Walborn, C. H. Monken, S. Pádua, P. H. S. Ribeiro, *Phys. Rep.* **2010**, *495*, 87.
[32] A. Anwar, C. Perumangatt, F. Steinlechner, T. Jennewein, A. Ling, *Rev. Sci. Instrum.* **2021**, *92*, 041101.
[33] M. Erhard, M. Krenn, A. Zeilinger, *Nat. Rev. Phys.* **2020**, *2*, 365.
[34] W. P. Grice, R. S. Bennink, D. S. Goodman, A. T. Ryan, *Phys. Rev. A* **2011**, *83*, 023810.
[35] A. Hochrainer, M. Lahiri, R. Lapkiewicz, G. B. Lemos, A. Zeilinger, *Proc. Natl. Acad. Sci. USA* **2017**, *114*, 1508.
[36] E. A. Ortega, J. Fuenzalida, M. Selimovic, K. Dovzhik, L. Achatz, S. Wengerowsky, R. F. Shiozaki, S. P. Neumann, M. Bohmann, R. Ursin, *JOSA B* **2023**, *40*, 165.
[37] C. K. Hong, Z. Y. Ou, L. Mandel, *Phys. Rev. Lett.* **1987**, *59*, 2044.
[38] F. Bouchard, A. Sit, Y. Zhang, R. Fickler, F. M. Miatto, Y. Yao, F. Sciarrino, E. Karimi, *Rep. Prog. Phys.* **2020**, *84*, 012402.
[39] L. Mandel, E. Wolf, *Rev. Mod. Phys.* **1965**, *37*, 231.
[40] H. J. Kimble, M. Dagenais, L. Mandel, *Phys. Rev. Lett.* **1977**, *39*, 691.
[41] L. Mandel, E. Wolf, *Optical Coherence and Quantum Optics*, Cambridge University Press, Oxford, UK **1995**.
[42] A. Zeilinger, T. Herzog, M. A. Horne, P. G. Kwiat, K. Mattle, H. Weinfurter, in *Coherence and Quantum Optics VII*, (Eds.: J. H. Eberly, L. Mandel, E. Wolf), Springer US, New York **1996**, pp. 305–312.
[43] B. Yurke, S. L. McCall, J. R. Klauder, *Phys. Rev. A* **1986**, *33*, 4033.
[44] A. Hochrainer, M. Lahiri, M. Erhard, M. Krenn, A. Zeilinger, *Rev. Mod. Phys.* **2022**, *94*, 025007.
[45] S.-Y. Baek, Y.-H. Kim, *Phys. Rev. A* **2009**, *80*, 033814.
[46] X. Y. Zou, T. Grayson, G. A. Barbosa, L. Mandel, *Phys. Rev. A* **1993**, *47*, 2293.
[47] G. A. Barbosa, *Phys. Rev. A* **1993**, *48*, 4730.
[48] T. P. Grayson, G. A. Barbosa, *Phys. Rev. A* **1994**, *49*, 2948.
[49] M. O. Scully, K. Drühl, *Phys. Rev. A* **1982**, *25*, 2208.
[50] T. J. Herzog, P. G. Kwiat, H. Weinfurter, A. Zeilinger, *Phys. Rev. Lett.* **1995**, *75*, 3034.
[51] H. M. Wiseman, K. Mølmer, *Phys. Lett. A* **2000**, *270*, 245.
[52] D. V. Strekalov, A. V. Sergienko, D. N. Klyshko, Y. H. Shih, *Phys. Rev. Lett.* **1995**, *74*, 3600.
[53] T. B. Pittman, Y. H. Shih, D. V. Strekalov, A. V. Sergienko, *Phys. Rev. A* **1995**, *52*, R3429.
[54] R. S. Bennink, S. J. Bentley, R. W. Boyd, *Phys. Rev. Lett.* **2002**, *89*, 113601.
[55] R. S. Aspden, D. S. Tasca, R. W. Boyd, M. J. Padgett, *New J. Phys.* **2013**, *15*, 073032.
[56] R. S. Bennink, S. J. Bentley, R. W. Boyd, J. C. Howell, *Phys. Rev. Lett.* **2004**, *92*, 033601.
[57] K. W. C. Chan, M. N. O'Sullivan, R. W. Boyd, *Phys. Rev. A* **2009**, *79*, 033808.
[58] P. A. Moreau, E. Toninelli, P. A. Morris, R. S. Aspden, T. Gregory, G. Spalding, R. W. Boyd, M. J. Padgett, *Opt. Express* **2018**, *26*, 7528.
[59] M. Lahiri, R. Lapkiewicz, G. B. Lemos, A. Zeilinger, *Phys. Rev. A* **2015**, *92*, 013832.
[60] A. C. Cardoso, L. P. Berruezo, D. F. Ávila, G. B. Lemos, W. M. Pimenta, C. H. Monken, P. L. Saldanha, S. Pádua, *Phys. Rev. A* **2018**, *97*, 033827.

2300353 (26 of 29)

**ADVANCED
SCIENCE NEWS**

www.advancedsciencenews.com

**ADVANCED
QUANTUM
TECHNOLOGIES**

www.advquantumtech.com

[61] M. Huang, D. Wu, H. Ren, L. Shen, T. Hawkins, J. Ballato, U. Gibson, M. Beresna, R. Slavík, J. Sipe, M. Liscidini, A. C. Peacock, *Photonics Res.* **2023**, *11*, 137.

[62] M. Lahiri, A. Hochrainer, R. Lapkiewicz, G. B. Lemos, A. Zeilinger, *Phys. Rev. A* **2017**, *96*, 013822.

[63] A. Vega, E. A. Santos, J. Fuenzalida, M. Gilaberte Basset, T. Pertsch, M. Gräfe, S. Saravi, F. Setzpfandt, *Phys. Rev. Res.* **2022**, *4*, 033252.

[64] A. Rojas-Santana, G. J. Machado, D. Lopez-Mago, J. P. Torres, *Phys. Rev. A* **2020**, *102*, 053711.

[65] J. Fuenzalida, A. Hochrainer, G. B. Lemos, E. A. Ortega, R. Lapkiewicz, M. Lahiri, A. Zeilinger, *Quantum* **2022**, *6*, 646.

[66] A. Gatti, E. Brambilla, L. A. Lugiato, *Phys. Rev. Lett.* **2003**, *90*, 133603.

[67] However, there is a third type of correlation between far field and near field.[66]

[68] B. Viswanathan, G. B. Lemos, M. Lahiri, *Opt. Lett.* **2021**, *46*, 3496.

[69] I. Kviatkovsky, H. M. Chrzanowski, S. Ramelow, *Opt. Express* **2022**, *30*, 5916.

[70] M. Gilaberte Basset, R. Sondenheimer, J. Fuenzalida, A. Vega, S. Töpfer, E. A. Santos, S. Saravi, F. Setzpfandt, F. Steinlechner, M. Gräfe, *Phys. Rev. A* **2023**, *108*, 052610.

[71] W. Zhang, R. Fickler, E. Giese, L. Chen, R. W. Boyd, *Opt. Express* **2019**, *27*, 20745.

[72] H. Defienne, S. Gigan, *Phys. Rev. A* **2019**, *99*, 053831.

[73] C. H. Monken, P. H. S. Ribeiro, S. Pádua, *Phys. Rev. A* **1998**, *57*, 3123.

[74] A. A. Harms, A. Zeilinger, *Phys. Med. Biol.* **1977**, *22*, 70.

[75] G. D. Boreman, *Modulation Transfer Function in Optical and Electro-Optical Systems*, vol. *4*, SPIE Press, Bellingham, WA **2001**.

[76] M. Born, E. Wolf, *Principles of Optics: Electromagnetic Theory of Propagation, Interference, and Diffraction of Light*, Elsevier, Cham, Switzerland **2013**.

[77] A. V. Paterova, H. Yang, Z. S. D. Toa, L. A. Krivitsky, *Appl. Phys. Lett.* **2020**, *117*, 054004.

[78] A. V. Paterova, D. A. Kalashnikov, E. Khaidarov, H. Yang, T. W. W. Mass, R. Paniagua-Domínguez, A. I. Kuznetsov, L. A. Krivitsky, *Nanophotonics* **2021**, *10*, 1775.

[79] N. R. Gemmell, J. Flórez, E. Pearce, O. Czerwinski, C. C. Phillips, R. F. Oulton, A. S. Clark, *Phys. Rev. Appl.* **2023**, *19*, 054019.

[80] E. Pearce, N. R. Gemmell, J. Flórez, J. Ding, R. F. Oulton, A. S. Clark, C. C. Phillips, *Opt. Continuum* **2023**, *2*, 2386.

[81] B. Viswanathan, G. B. Lemos, M. Lahiri, *Opt. Express* **2021**, *29*, 38185.

[82] A. Fedotova, L. Carletti, A. Zilli, F. Setzpfandt, I. Staude, A. Toma, M. Finazzi, C. De Angelis, T. Pertsch, D. N. Neshev, M. Celebrano, *ACS Photonics* **2022**, *9*, 3745.

[83] D. Gabor, *Nature* **1948**, *161*, 777.

[84] P. Marquet, C. Depeursinge, P. J. Magistretti, *Neurophotonics* **2014**, *1*, 020901.

[85] X. Quan, D. Kato, V. Daria, O. Matoba, H. Wake, *Neurosci. Res.* **2022**, *179*, 57.

[86] R. Chrapkiewicz, M. Jachura, K. Banaszek, W. Wasilewski, *Nat. Photon.* **2016**, *10*, 576.

[87] H. Defienne, B. Ndagano, A. Lyons, D. Faccio, *Nat. Phys.* **2021**, *17*, 591.

[88] A. N. Black, L. D. Nguyen, B. Braverman, K. T. Crampton, J. E. Evans, R. W. Boyd, *Optica* **2023**, *10*, 952.

[89] See also ref. [88].

[90] I. Yamaguchi, T. Zhang, *Opt. Lett.* **1997**, *22*, 1268.

[91] S. Lloyd, *Science* **2008**, *321*, 1463.

[92] S.-H. Tan, B. I. Erkmen, V. Giovannetti, S. Guha, S. Lloyd, L. Maccone, S. Pirandola, J. H. Shapiro, *Phys. Rev. Lett.* **2008**, *101*, 253601.

[93] E. Lopaeva, I. R. Berchera, I. P. Degiovanni, S. Olivares, G. Brida, M. Genovese, *Phys. Rev. Lett.* **2013**, *110*, 153603.

[94] J.-W. Pan, C. Simon, Č. Brukner, A. Zeilinger, *Nature* **2001**, *410*, 1067.

[95] H. Defienne, M. Reichert, J. W. Fleischer, D. Faccio, *Sci. Adv.* **2019**, *5*, eaax0307.

[96] T. Gregory, P. A. Moreau, E. Toninelli, M. J. Padgett, *Sci. Adv.* **2020**, *6*, eaay2652.

[97] D. G. England, B. Balaji, B. J. Sussman, *Phys. Rev. A* **2019**, *99*, 023828.

[98] Y. Zhang, D. England, A. Nomerotski, P. Svihra, S. Ferrante, P. Hockett, B. Sussman, *Phys. Rev. A* **2020**, *101*, 053808.

[99] J. Zhao, A. Lyons, A. C. Ulku, H. Defienne, D. Faccio, E. Charbon, *Opt. Express* **2022**, *30*, 3675.

[100] A. Paterova, H. Yang, C. An, D. Kalashnikov, L. Krivitsky, *Opt. Express* **2019**, *27*, 2589.

[101] A. Paterova, S. Lung, D. A. Kalashnikov, L. A. Krivitsky, *Sci. Rep.* **2017**, *7*, 1.

[102] S. K. Lee, T. H. Yoon, M. Cho, *Opt. Express* **2019**, *27*, 14853.

[103] S. K. Lee, T. H. Yoon, M. Cho, *Phys. Rev. Appl.* **2020**, *14*, 014045.

[104] A. C. Cardoso, H. Zhou, S. K. Joshi, J. G. Rarity, "Enhancing methane sensors by sensing without detection", *arxiv* **2022**, arxiv:2209.15289.

[105] C. Lindner, J. Kunz, S. J. Herr, J. Kießling, S. Wolf, F. Kühnemann, *APL Photonics* **2023**, *8*, 051301.

[106] Z. S. Toa, M. V. Chekhova, L. A. Krivitsky, A. V. Paterova, *Opt. Express* **2023**, *31*, 7265.

[107] C. Lindner, S. Wolf, J. Kiessling, F. Kühnemann, *Opt. Express* **2020**, *28*, 4426.

[108] C. Lindner, J. Kunz, S. J. Herr, S. Wolf, J. Kießling, F. Kühnemann, *Opt. Express* **2021**, *29*, 4035.

[109] C. Lindner, J. Kunz, S. J. Herr, J. Kiessling, S. Wolf, F. Kühnemann, *Opt. Continuum* **2022**, *1*, 189.

[110] P. Kaufmann, H. M. Chrzanowski, A. Vanselow, S. Ramelow, *Opt. Express* **2022**, *30*, 5926.

[111] Y. Mukai, M. Arahata, T. Tashima, R. Okamoto, S. Takeuchi, *Phys. Rev. Appl.* **2021**, *15*, 034019.

[112] Y. Mukai, R. Okamoto, S. Takeuchi, *Opt. Express* **2022**, *30*, 22624.

[113] D. Huang, E. A. Swanson, C. P. Lin, J. S. Schuman, W. G. Stinson, W. Chang, M. R. Hee, T. Flotte, K. Gregory, C. A. Puliafito, J. G. Fujimoto, *Science* **1991**, *254*, 1178.

[114] A. Rojas-Santana, G. J. Machado, D. Lopez-Mago, J. P. Torres, *Phys. Rev. A* **2020**, *102*, 053711.

[115] G. J. Machado, G. Frascella, J. P. Torres, M. V. Chekhova, *Appl. Phys. Lett.* **2020**, *117*, 094002.

[116] A. Vanselow, P. Kaufmann, I. Zorin, B. Heise, H. M. Chrzanowski, S. Ramelow, *Optica* **2020**, *7*, 1729.

[117] A. Rojas-Santana, G. J. Machado, M. V. Chekhova, D. Lopez-Mago, J. P. Torres, *Phys. Rev. A* **2022**, *106*, 033702.

[118] B. Haase, M. Kutas, F. Riexinger, P. Bickert, A. Keil, D. Molter, M. Bortz, G. Von Freymann, *Opt. Express* **2019**, *27*, 7458.

[119] G. B. Lemos, R. Lapkiewicz, A. Hochrainer, M. Lahiri, A. Zeilinger, *Phys. Rev. Lett.* **2023**, *130*, 090202.

[120] M. Lahiri, R. Lapkiewicz, A. Hochrainer, G. B. Lemos, A. Zeilinger, *Phys. Rev. A* **2021**, *104*, 013704.

[121] J. Fuenzalida, J. Kysela, K. Dovzhik, G. B. Lemos, A. Hochrainer, M. Lahiri, A. Zeilinger, *Phys. Rev. A* **2024**, *109*, 022413.

[122] M. A. Nielsen, I. Chuang, *Quantum Computation and Quantum Information*, Cambridge University Press, Cambridge, MA **2002**.

[123] M. Lahiri, A. Hochrainer, R. Lapkiewicz, G. B. Lemos, A. Zeilinger, *Phys. Rev. A* **2017**, *95*, 033816.

[124] J. H. Shapiro, D. Venkatraman, F. N. C. Wong, *Sci. Rep.* **2015**, *5*, 10329.

[125] A. V. Belinsky, D. N. Klyshko, *Phys. Lett. A* **1992**, *166*, 303.

[126] M. I. Kolobov, E. Giese, S. Lemieux, R. Fickler, R. W. Boyd, *J. Opt.* **2017**, *19*, 054003.

[127] J. Le Gouët, D. Venkatraman, F. N. C. Wong, J. H. Shapiro, *Opt. Express* **2009**, *17*, 17874.

[128] Such interferometers have not necessarily be performed with optical systems, but have also been implemented by atomic modes instead.

[129] D. Linnemann, H. Strobel, W. Muessel, J. Schulz, R. J. Lewis-Swan, K. V. Kheruntsyan, M. K. Oberthaler, *Phys. Rev. Lett.* **2016**, *117*, 013001.

[130] S. Schaffrath, D. Derr, M. Gräfe, E. Giese, *New J. Phys.* **2024**, *26*, 023018.

[131] A. M. Marino, N. V. Corzo Trejo, P. D. Lett, *Phys. Rev. A* **2012**, *86*, 023844.

[132] M. Manceau, G. Leuchs, F. Khalili, M. Chekhova, *Phys. Rev. Lett.* **2017**, *119*, 223604.

[133] E. Giese, S. Lemieux, M. Manceau, R. Fickler, R. W. Boyd, *Phys. Rev. A* **2017**, *96*, 053863.

[134] S. S. Szigeti, R. J. Lewis-Swan, S. A. Haine, *Phys. Rev. Lett.* **2017**, *118*, 150401.

[135] N. R. Miller, S. Ramelow, W. N. Plick, *Quantum* **2021**, *5*, 458.

[136] G. Frascella, E. E. Mikhailov, N. Takanashi, R. V. Zakharov, O. V. Tikhonova, M. V. Chekhova, *Optica* **2019**, *6*, 1233.

[137] D. N. Klyshko, *Photons and Nonlinear Optics*, Gordon and Breach, Boca Raton, FL **1989**.

[138] V. Boyer, A. Marino, P. Lett, *Phys. Rev. Lett.* **2008**, *100*, 143601.

[139] S. Lemieux, E. Giese, R. Fickler, M. V. Chekhova, R. W. Boyd, *Nat. Phys.* **2019**, *15*, 529.

[140] O. Jedrkiewicz, Y.-K. Jiang, E. Brambilla, A. Gatti, M. Bache, L. A. Lugiato, P. Di Trapani, *Phys. Rev. Lett.* **2004**, *93*, 243601.

[141] M. Bondani, A. Allevi, G. Zambra, M. G. A. Paris, A. Andreoni, *Phys. Rev. A* **2007**, *76*, 013833.

[142] G. Brida, L. Caspani, A. Gatti, M. Genovese, A. Meda, I. R. Berchera, *Phys. Rev. Lett.* **2009**, *102*, 213602.

[143] M. V. Chekhova, G. Leuchs, M. Żukowski, *Opt. Commun.* **2015**, *337*, 27.

[144] I. N. Agafonov, M. V. Chekhova, G. Leuchs, *Phys. Rev. A* **2010**, *82*, 011801.

[145] A. M. Pérez, T. S. Iskhakov, P. Sharapova, S. Lemieux, O. V. Tikhonova, M. V. Chekhova, G. Leuchs, *Opt. Lett.* **2014**, *39*, 2403.

[146] S. Lemieux, M. Manceau, P. R. Sharapova, O. V. Tikhonova, R. W. Boyd, G. Leuchs, M. V. Chekhova, *Phys. Rev. Lett.* **2016**, *117*, 183601.

[147] N. Quesada, J. E. Sipe, *Phys. Rev. A* **2014**, *90*, 063840.

[148] A. Christ, B. Brecht, W. Mauerer, C. Silberhorn, *New J. Phys.* **2013**, *15*, 053038.

[149] P. Sharapova, A. M. Pérez, O. V. Tikhonova, M. V. Chekhova, *Phys. Rev. A* **2015**, *91*, 043816.

[150] P. R. Sharapova, O. V. Tikhonova, S. Lemieux, R. W. Boyd, M. V. Chekhova, *Phys. Rev. A* **2018**, *97*, 053827.

[151] P. R. Sharapova, G. Frascella, M. Riabinin, A. M. Pérez, O. V. Tikhonova, S. Lemieux, R. W. Boyd, G. Leuchs, M. V. Chekhova, *Phys. Rev. Res.* **2020**, *2*, 013371.

[152] A. Ferreri, M. Santandrea, M. Stefszky, K. H. Luo, H. Herrmann, C. Silberhorn, P. R. Sharapova, *Quantum* **2021**, *5*, 461.

[153] D. Scharwald, T. Meier, P. R. Sharapova, *Phys. Rev. Research* **2023**, *5*, 043158.

[154] K. Hashimoto, D. B. Horoshko, M. V. Chekhova, *Adv. Quantum Technol.* **2023**, https://doi.org/10.1002/qute.202300299.

[155] W. N. Plick, J. P. Dowling, G. S. Agarwal, *New J. Phys.* **2010**, *12*, 083014.

[156] A. Heuer, R. Menzel, P. W. Milonni, *Phys. Rev. A* **2015**, *92*, 033834.

[157] W. Du, J. Jia, J. F. Chen, Z. Y. Ou, W. Zhang, *Opt. Lett.* **2018**, *43*, 1051.

[158] J. Liu, Y. Wang, M. Zhang, J. Wang, D. Wei, H. Gao, *Opt. Express* **2020**, *28*, 39443.

[159] F. Hudelist, J. Kong, C. Liu, J. Jing, Z. Y. Ou, W. Zhang, *Nat. Commun.* **2014**, *5*, 3049.

[160] F. Riexinger, M. Kutas, B. Haase, M. Bortz, G. von Freymann, *Laser Photonics Rev.* **2023**, 2200945.

[161] C. Yang, Z.-Y. Zhou, L.-L. Wang, Y. Li, S.-K. Liu, Z. Ge, X.-C. Zhang, Q. Tang, G.-C. Guo, B.-S. Shi, *Opt. Express* **2021**, *29*, 32006.
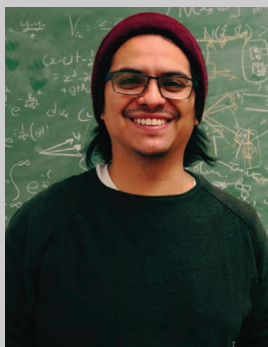
Jorge Fuenzalida studied physics at the University of Concepcion, Chile. He received his Ph.D. in Physics from the University of Vienna, Austria, for his work with nonlinear interferometers. Later, he performed a postdoc at the Fraunhofer IOF, Germany, focusing on quantum imaging. He is currently a postdoc at the Technical University of Darmstadt, Germany. His research interests include nonlinear interferometry, entanglement, quantum imaging, and quantum information science.

Enno Giese received his doctorate in 2015 at Ulm University, working theoretically on matter-wave diffraction. He received the Akademiepreis of the Heidelberg Academy of Sciences and Humanities for his research. Subsequently, he held a postdoctoral position at the University of Ottawa, studying quantum nonlinear optics, quantum imaging, and nonlinear interferometry. Next, he focused on matter-wave interferometry in microgravity and for tests of relativity. In 2021, he was appointed Professor for Theoretical Quantum Optics at the Institute for Applied Physics at TU Darmstadt. He possesses years of experience in fundamental aspects and applications of atom interferometry and quantum imaging.

**ADVANCED
SCIENCE NEWS**

www.advancedsciencenews.com

**ADVANCED
QUANTUM
TECHNOLOGIES**

www.advquantumtech.com

Markus Gräfe has been a full professor at the Technical University of Darmstadt since 2022. He leads the Experimental Solid State Quantum Optics Group at the Institute of Applied Physics. Before, he was a research group leader in quantum imaging at Fraunhofer IOF. He started this position in 2017 after his PhD, where he was working on integrated photonic quantum walks. His work was awarded with the Applied Photonics Award in 2018. He currently conducts research in the fields of quantum imaging, quantum walks, and quantum photonic sources.